Wavenumber-frequency deconvolution of aeroacoustic microphone phased array data of arbitrary coherence

Christopher J. Bahr[a,*], Louis N. Cattafesta[b]

[a] *Aeroacoustics Branch, NASA Langley Research Center, Hampton, VA, USA*
[b] *Florida Center for Advanced Aero-Propulsion (FCAAP), Department of Mechanical Engineering, Florida State University, Tallahassee, FL, USA*

Abstract

Deconvolution of aeroacoustic data acquired with microphone phased arrays is a computationally-challenging task for distributed sources with arbitrary coherence. A new technique for performing such deconvolution is proposed. This technique relies on analysis of the array data in the wavenumber-frequency domain, allowing for fast convolution and reduced storage requirements when compared to traditional coherent deconvolution. A positive semidefinite constraint for the iterative deconvolution procedure is implemented and shows improved behavior in terms of quantifiable convergence metrics when compared to a standalone covariance inequality constraint. A series of simulations validates the method's ability to resolve coherence and phase angle relationships between partially-coherent sources, as well as determines convergence criteria for deconvolution analysis. Simulations for point sources near the microphone phased array show potential for handling such data in the wavenumber-frequency domain. In particular, a physics-based integration boundary calculation is described, and can successfully isolate sources and track the appropriate integration bounds with and without the presence of flow. Magnitude and phase relationships between multiple sources are successfully extracted. Limitations of the deconvolution technique are determined from the simulations, particularly in the context of a simulated acoustic field in a closed test section wind tunnel with strong boundary layer contamination. A final application to a trailing edge noise experiment conducted in an open-jet wind tunnel matches best estimates of acoustic levels from traditional calculation methods and qualitatively assesses the coherence characteristics of the trailing edge noise source.

Keywords:
phased array, beamforming, deconvolution, wavenumber-frequency

Nomenclature

Dimensions

*Corresponding author
Email address: christopher.j.bahr@nasa.gov (Christopher J. Bahr)

$k_x, k_y, k_z, k_\xi, k_\eta$	wavenumber vector components and two-dimensional conjugates, m^{-1}
x, y, z, ξ, η	spatial dimensions and two-dimensional conjugates, m
r, θ, ϕ	spherical coordinates (radius, inclination angle, azimuth angle), deg
t	time, s

Symbols

a	relaxation parameter
$\mathbf{A}$	system matrix
$\mathbf{B}$, $\mathbf{C}$, $\mathbf{D}$	matrices used in iteration stability analysis
c_0	isentropic speed of sound, m/s
$\mathbf{e}\left(k_x, k_y\right)$	row vector of wavenumber transform terms
E	expected value operation
$\hat{e}$	unit vector component
f	temporal frequency, Hz
$\mathbf{G}$	cross-spectral matrix, Pa^2
I	matrix index
$\mathbf{I}$	identity matrix
J	matrix index
j	imaginary unit
$k_{max,()}$	maximum considered wavenumber in a given dimension, m^{-1}
$k_{min,()}$	minimum considered wavenumber in a given dimension, m^{-1}
k_0	acoustic wavenumber based on frequency and speed of sound, $k_0 = f/c_0$, m^{-1}
$\ell^{()}$	()-norm of a vector
M	Mach number
N	total number of microphones in an array
n_g	total number of grid points in a beam map
$n_{k,()}$	number of grid points in a given dimension in the wavenumber domain
$n_{s,()}$	number of grid points in a given dimension required for linear convolution
$\mathbf{p}$	column vector of measured pressures, Pa
$p\left(x, y\right)$	sampled pressure field on an array face, Pa
p_m	pressure sampled at microphone m for a given narrowband frequency, Pa
$\tilde{p}\left(k_x, k_y\right)$	wavenumber transform of sampled pressure field, Pa
$P\left(x, y, \xi, \eta\right)$	measured spatial pressure covariance, Pa^2
$\tilde{P}\left(k_x, k_y, k_\xi, k_\eta\right)$	measured wavenumber-frequency covariance, Pa^2

$q\left(x, y\right)$	true pressure field on array face, Pa
$\tilde{q}\left(k_x, k_y\right)$	wavenumber transform of true pressure field, Pa
$\tilde{Q}\left(k_x, k_y, k_\xi, k_\eta\right)$	wavenumber-frequency covariance of true pressure field, Pa^2
$\hat{Q}$	forward spatial Fourier transform of $\tilde{Q}$, Pa^2
$\mathbf{Q}$	Covariance matrix form of $\tilde{Q}$
r_σ	matrix spectral radius
$\tilde{R}\left(k_x, k_y, k_\xi, k_\eta\right)$	convolution of $\tilde{Q}$ with $\tilde{S}$, Pa^2
$\hat{R}$	forward spatial Fourier transform of $\tilde{R}$, Pa^2
$\mathbb{R}^{\mathrm{n}}$	real number set in n dimensions
$s\left(x, y\right)$	spatial array sampling function
$\tilde{s}\left(k_x, k_y\right)$	wavenumber transform of array sampling function
$\tilde{S}\left(k_x, k_y, k_\xi, k_\eta\right)$	wavenumber-frequency covariance array sampling function
$\hat{S}$	forward spatial Fourier transform of $\tilde{S}$
T	time series block length used in ensemble-averaging, s
U	moving medium mean velocity (signed), m/s
u	normalized ℓ^2 algorithm residual
v	normalized ℓ^1 change in solution
$\vec{v}$	arbitrary velocity vector, m/s
w	3-dB beamwidth of array sampling function in the wavenumber domain, m^{-1}
$\mathbf{x}$	column vector of sources
$\mathbf{y}$	column vector of observations
$\Delta k_{()}$	grid point spacing in a given dimension in the wavenumber domain, m^{-1}
$\delta\left(\vec{x} - \vec{x}_m\right)$	Dirac delta function
γ^2	coherence-squared function
λ	eigenvalue
Ψ	wavenumber filter weighting function

Subscripts and Superscripts

$()_g$	group velocity vector term
$()_p$	phase velocity vector term
$()^H$	Hermitian transpose
$()^{(i)}$	current iteration number
$()^*$	complex conjugate
$()'$	shifted coordinate

1. Introduction

In aeroacoustic wind tunnel testing, the limitations of conventional beamforming with microphone phased arrays impede the ability to extract quantitative information from beam maps. Simple integration techniques can be used to provide approximate field values, but in general the inverse problem of beam map deconvolution must be solved to extract quantitative information from array data [1]. Many frequency-domain deconvolution algorithms exist for incoherent source fields, for example DAMAS [1], DAMAS2 [2], SC-DAMAS [3], and CLEAN-SC [4]. However, when a source field contains regions of coherence, there are fewer algorithm selections. Methods such as MACS are computationally reasonable but assume a sparse source field [5]. Similarly, LORE is a quick algorithm but only solves for a subset of the scan grid [6]. DAMAS-C has the potential to evaluate coherent sources over the entire source region of interest, but application is computationally challenging even for small source regions [7]. Generalized inverse methods involving either eigenvalue subsets of the measured cross-spectral matrix (CSM) [8] or the entire CSM of an array data set [9] may resolve distributed, partially-coherent source fields, but the range of applicability and limitations of these methods have yet to be completely addressed.

In microphone phased array analysis, deconvolution is the constrained inverse of the linear convolution of an array's sampling response with the true source field of interest. When an array is steered to a set of discrete scan locations, the array output can be stored in a vector of observations $\mathbf{y}$. These observations can be modeled as a vector of source variances $\mathbf{x}$ multiplied by the matrix $\mathbf{A}$ containing the response characteristics. Assuming the observations are uncontaminated by measurement noise, this is simply

$$\mathbf{y} = \mathbf{A}\mathbf{x}. \tag{1}$$

Deconvolution inverts this system to solve for $\mathbf{x}$. For many problems of interest, $\mathbf{A}$ is nearly singular so direct inversion is infeasible. Algorithms such as DAMAS and DAMAS2 handle the solution process iteratively through a Gauss-Seidel or Jacobi procedure, respectively, where $\mathbf{x} \geq 0$ is enforced between iterations under the assumption of incoherence between sources. DAMAS2 applies a shift-invariance assumption, tantamount to assuming that the source field consists of plane waves. This allows the use of a Fourier-based technique to perform a fast convolution of $\mathbf{x}$ with $\mathbf{A}$ rather than the full matrix-vector multiplication [2]. Individual iterations of DAMAS2 are significantly faster than DAMAS for a given problem, but depending on the validity of the shift-invariance assumption and desired convergence criteria, more iterations of DAMAS2 may be required and accuracy may be limited. A smoothing filter may be used with DAMAS2 to improve conditioning and accelerate convergence.

Deconvolution assuming arbitrary coherence, where elements of $\mathbf{x}$ may be statistically related to each other, is also modeled by Eq. (1). In this case, $\mathbf{x}$ and $\mathbf{y}$ include not only the source and observation variances of grid points but also the covariances between grid points. $\mathbf{A}$ must then account for the influence of all source variances and covariances on a given observation variance or covariance. Constraints on these additional elements may be defined by a covariance inequality [10] rather than a positivity constraint, although an alternative which shows improved behavior is proposed in this work. In general the terms of $\mathbf{x}$ are complex. Unfortunately, when allowing for arbitrary coherence the computational scaling of deconvolution becomes problematic. If a scan grid of interest has n_g grid points, $\mathbf{x}$ and $\mathbf{y}$ each have n_g^2 elements and $\mathbf{A}$ has n_g^4 elements. For example, a 20×20 beam map has $n_g = 400$ grid points. This means $\mathbf{x}$ and $\mathbf{y}$ each have $n_g^2 = 1.6 \times 10^5$ elements to account for all possible variance and covariance terms, meaning $\mathbf{A}$ has $n_g^4 = 2.56 \times 10^{10}$, or 25.6 billion, elements. Conjugate-symmetry reduces the number of independent covariance terms by a factor of two, but the scaling remains. To compute the covariance relationships between every pairing of grid points in the beam map, $\mathbf{A}$ must be treated as, in general, a non-sparse matrix (although many terms may be orders of magnitude smaller than the maximum matrix element). While a matrix of this size is possible to generate and store, it does not lend itself to efficient computation, and the scaling problem excludes analysis of larger grids. In-situ recalculation of the terms of $\mathbf{A}$ has been successfully applied, though the full calculation is expensive [11].

To make the evaluation of $\mathbf{Ax}$ more tractable for this form of deconvolution, it would be helpful to define the problem such that every element of $\mathbf{A}$ does not need to be simultaneously computed and stored. Additionally, a fast convolution technique similar to that used by DAMAS2 is desired. A formulation of the coherent deconvolution process which accomplishes these objectives is presented here. A shift-invariance assumption, where the element of $\mathbf{A}$ relating a given element of $\mathbf{y}$ to an element of $\mathbf{x}$ is dependent only on the separation of the two points in the analysis domain, is applied to the coherent problem. Shift-invariance has previously been applied to the DAMAS-C problem in the spatial domain [11]. It is done here by analyzing the array data in the wavenumber-frequency domain.

Analysis of array data in the wavenumber-frequency domain can be a powerful tool. An acoustic field from an arbitrary source can be expressed as the inverse transform of a plane wave expansion, or wavenumber-frequency representation, of the field [12]. It must be used with care, as both the approximation of the field by a discrete set of wavenumber vector components and the sampling limitations of a finite aperture, finite element count, non-uniformly spaced array not located in the near field of a source impede quantitative reconstruction of a general field. However, it allows the separation of supersonic (radiating) and subsonic (evanescent) components projected on an array face [13], giving the potential to separate acoustic and hydrodynamic waves in subsonic flows.

In this work, the general problem of a transformation of an arbitrary-coherence pressure field to the wavenumber-frequency domain is addressed Section 2. Implementation details such as algorithm structure and constraints, updated from previous work, are addressed in Section 3 along with potential methods for accelerating convergence. Section 4 presents two applications which are representative of possible aeroacoustic wind tunnel tests. The first is simulated data in a closed test section. The second is experimental data in an open-jet facility. The summary and conclusions follow in Section 5. The appendices contain a detailed simulated data study of the algorithm performance to determine its characteristics and limitations, in addition to detailing some data analysis techniques to assess use for non-planar acoustic wave fields.

2. Formulation

The wavenumber-frequency deconvolution problem is desired in a functionally-equivalent form of Eq. (1), where $\mathbf{y}$ is the wavenumber transform of the observed array data for a given narrowband frequency and $\mathbf{A}$ contains the model of the array sampling function. The desired form must include and account for both the variances of the individual wavenumber components and the covariances between wavenumber components of the wavenumber-frequency spectrum. The wavenumber domain array sampling function can be obtained from the physical space sampling function, which can be constructed in terms of sampling theory. This is done by modeling the array measurement process as the multiplication of the true pressure field in space by a distribution of delta functions corresponding to microphone locations in the array [14]. This multiplication in the spatial domain becomes an equivalent convolution in the Fourier transform of the spatial domain, or the wavenumber domain.

The sampling function applied to the pressure field on a planar array face defined at $z = 0$ is given by

$$s\left(x, y\right) = \sum_{m=1}^{N} \delta\left(x - x_m, y - y_m\right). \tag{2}$$

The sampled, temporally-Fourier transformed narrowband pressure field (frequency-dependence suppressed in the notation) is then given by

$$\begin{aligned} p\left(x, y\right) &= s\left(x, y\right) q\left(x, y\right) \\ &= \sum_{m=1}^{N} p_m \delta\left(x - x_m, y - y_m\right). \end{aligned} \tag{3}$$

The 2-D spatial Fourier transforms of these quantities are thus

$$\tilde{s}\left(k_x, k_y\right) = \iint_{\mathbb{R}^2} s\left(x, y\right) e^{j2\pi\left(k_x x + k_y y\right)} \,\mathrm{d}x \,\mathrm{d}y = \frac{1}{N} \sum_{m=1}^{N} e^{j2\pi\left(k_x x_m + k_y y_m\right)} \tag{4}$$

and

$$\begin{aligned} \tilde{p}\left(k_x, k_y\right) &= \iint_{\mathbb{R}^2} p\left(x, y\right) e^{j2\pi\left(k_x x + k_y y\right)} \,\mathrm{d}x \,\mathrm{d}y = \frac{1}{N} \sum_{m=1}^{N} p_m e^{j2\pi\left(k_x x_m + k_y y_m\right)} \\ &= \iint_{\mathbb{R}^2} \tilde{s}\left(k_x - k_x', k_y - k_y'\right) \tilde{q}\left(k_x', k_y'\right) \,\mathrm{d}k_x' \,\mathrm{d}k_y', \end{aligned} \tag{5}$$

where the normalization by N is included such that a unit-magnitude plane wave in physical space has unit magnitude in its peak wavenumber domain representation. Note that no k_z transform is performed as all microphones are assumed co-planar, common for many aeroacoustic wind tunnel tests, so no z-information is available. This is effectively evaluating the projection of a wave front propagating over the array face. Note that the following conventions are used in this work. The $+1$ sign in the complex exponential of the wavenumber transform is selected based on the assumption that temporal transforms have a -1 sign, following convention [15]. Also, spatial Fourier transforms in this work are scaled using wavenumbers of inverse length, rather than radians per unit length.

Eq. (5) is a formulation of the basic wavenumber pressure sampling problem for a deterministic fluctuating pressure field, or for a single block of data from a stochastic one. However, to properly handle the stochastic nature of typical pressure fields in aeroacoustics, auto- and cross-power spectral densities are used to represent the ensemble-average characteristics of the field. A CSM for a given narrowband frequency contains the variances and covariances, or elements of auto- and cross-spectral densities scaled by the narrowband bin width, of the array microphone measurements. The (one-sided) CSM is ensemble-averaged across many blocks of data and is represented by

$$\mathbf{G} = \frac{2}{T^2} E\left[\mathbf{p}\mathbf{p}^H\right] = \begin{bmatrix} E\left[p\left(x_1, y_1\right) p^*\left(x_1, y_1\right)\right] & \dots & E\left[p\left(x_1, y_1\right) p^*\left(x_N, y_N\right)\right] \\ \vdots & \ddots & \vdots \\ E\left[p\left(x_N, y_N\right) p^*\left(x_1, y_1\right)\right] & \dots & E\left[p\left(x_N, y_N\right) p^*\left(x_N, y_N\right)\right] \end{bmatrix}. \tag{6}$$

For a planar array, the CSM contains 4-D spatial covariance information,

$$P\left(x, y, \xi, \eta\right) = \frac{2}{T^2} E\left[p\left(x, y\right) p^*\left(\xi, \eta\right)\right]. \tag{7}$$

An equivalent covariance relationship in the wavenumber-frequency domain is desired. This would take the form of

$$\tilde{P}\left(k_x, k_y, k_\xi, k_\eta\right) = \frac{2}{T^2} E\left[\tilde{p}\left(k_x, k_y\right) \tilde{p}^*\left(k_\xi, k_\eta\right)\right] \tag{8}$$

and can be computed by substituting the first line of Eq. (5) into Eq. (8), giving

$$\begin{aligned} \tilde{P}\left(k_x, k_y, k_\xi, k_\eta\right) &= \frac{2}{T^2} E\left[\tilde{p}\left(k_x, k_y\right) \tilde{p}^*\left(k_\xi, k_\eta\right)\right] \\ &= \frac{2}{T^2} E\left[\frac{1}{N}\sum_{n=1}^{N} p_n e^{j2\pi\left(k_x x_n + k_y y_n\right)} \frac{1}{N}\sum_{m=1}^{N} p_m^* e^{-j2\pi\left(k_\xi \xi_m + k_\eta \eta_m\right)}\right] \\ &= \frac{1}{N^2}\sum_{n=1}^{N}\sum_{m=1}^{N} \frac{2}{T^2} E\left[p_n p_m^*\right] e^{j2\pi\left(k_x x_n + k_y y_n\right)} e^{-j2\pi\left(k_\xi \xi_m + k_\eta \eta_m\right)}. \end{aligned} \tag{9}$$

When $k_\xi = k_x$ and $k_\eta = k_y$, Eq. (9) reduces to the wavenumber variance. This expression of the wavenumber variance matches Eq. 12 given by Capon [16] for uniform element weighting. The full equation, as a 4-D covariance relationship of 2-D wavenumber-frequency information, captures any coherence relationships between regions in the wavenumber domain. The term $E\left[p_n p_m^*\right]$ in Eq. (9) is an entry in the CSM. Thus, in linear algebra terms, the double-summation can be re-expressed as

$$\tilde{P}\left(k_x, k_y, k_\xi, k_\eta\right) = \frac{1}{N^2} \mathbf{e}\left(k_x, k_y\right) \mathbf{G} \mathbf{e}^H\left(k_\xi, k_\eta\right), \tag{10}$$

with row vector $\mathbf{e}(k_x, k_y)$ given by

$$\boldsymbol{e}(k_x, k_y) = \begin{bmatrix} e^{j2\pi(k_x x_1 + k_y y_1)} & e^{j2\pi(k_x x_2 + k_y y_2)} & \dots & e^{j2\pi(k_x x_N + k_y y_N)} \end{bmatrix}. \tag{11}$$

Similarly, the wavenumber covariance sampling function can be constructed as

$$\tilde{S}(k_x, k_y, k_\xi, k_\eta) = \frac{1}{N^2}\mathbf{e}(k_x, k_y) \begin{bmatrix} 1 & \dots & 1 \\ \vdots & \ddots & \vdots \\ 1 & \dots & 1 \end{bmatrix} \mathbf{e}^H(k_\xi, k_\eta). \tag{12}$$

Note that when diagonal removal [17] is applied, where $m = n$ terms of the CSM are neglected, the normalization should change from N^2 to $N^2 - N$ to maintain unit response.

A 4-D convolution statement equivalent to the second line of Eq. (5) can be constructed by substituting the second line of Eq. (5) into Eq. (8),

$$\begin{aligned} \tilde{P}(k_x, k_y, k_\xi, k_\eta) &= \frac{2}{T^2} E\left[\tilde{p}(k_x, k_y)\, \tilde{p}^*(k_\xi, k_\eta)\right] \\ &= \frac{2}{T^2} E\left[\iint_{\mathbb{R}^2} \tilde{s}\left(k_x - k_x', k_y - k_y'\right) \tilde{q}\left(k_x', k_y'\right)\, \mathrm{d}k_x'\, \mathrm{d}k_y' \times \right. \\ &\qquad \left. \iint_{\mathbb{R}^2} \tilde{s}^*\left(k_\xi - k_\xi', k_\eta - k_\eta'\right) \tilde{q}^*\left(k_\xi', k_\eta'\right)\, \mathrm{d}k_\xi'\, \mathrm{d}k_\eta' \right] \\ &= \iint_{\mathbb{R}^2} \iint_{\mathbb{R}^2} \tilde{s}\left(k_x - k_x', k_y - k_y'\right) \tilde{s}^*\left(k_\xi - k_\xi', k_\eta - k_\eta'\right) \times \\ &\qquad \frac{2}{T^2} E\left[\tilde{q}\left(k_x', k_y'\right) \tilde{q}^*\left(k_\xi', k_\eta'\right)\right] \mathrm{d}k_x'\, \mathrm{d}k_y'\, \mathrm{d}k_\xi'\, \mathrm{d}k_\eta' \\ &= \iiiint_{\mathbb{R}^4} \tilde{S}\left(k_x - k_x', k_y - k_y', k_\xi - k_\xi', k_\eta - k_\eta'\right) \tilde{Q}\left(k_x', k_y', k_\xi', k_\eta'\right) \mathrm{d}k_x'\, \mathrm{d}k_y'\, \mathrm{d}k_\xi'\, \mathrm{d}k_\eta'. \end{aligned} \tag{13}$$

This statement allows for a shift-invariant model of $\mathbf{A}$ in Eq. (1). When $\tilde{P}$ is constructed on a discrete grid, it can be stored in the observation vector $\mathbf{y}$. The source field $\tilde{Q}$ becomes the solution vector $\mathbf{x}$, and the problem of interest is to find the source field which best fits the data in the observation vector, obeying the given constraints and avoiding explicit computation or storage of $\mathbf{A}$.

3. Implementation

To solve this problem, $\tilde{P}$ and $\tilde{S}$ are first constructed for a discrete set of coordinates in the wavenumber domain. The coordinates are equally-spaced within a given dimension. Each coordinate set spans $k_{()} = \left[k_{min,()} : \Delta k_{()} : k_{max,()}\right]$ for a total grid size of $n_{k,x} \times n_{k,y} \times n_{k,\xi} \times n_{k,\eta}$. Note that the notation $n_{k,x}$ indicates the number of points in the k_x dimension, and is used similarly for other dimensions. For a proper covariance analysis, the k_ξ grid must match the k_x grid and the k_η grid must match the k_y grid, as these are conjugate pairings. This leads to a covariance matrix of size $(n_{k,x} \times n_{k,y}) \times (n_{k,\xi} \times n_{k,\eta})$. The selection of the parameters $k_{min,()}$, $k_{max,()}$, $\Delta k_{()}$ and $n_{k,()}$ is discussed subsequently and is dependent on the array, the problem of interest, and available computational resources.

An iterative solution of Eq. (1) can take the form of

$$\mathbf{x}^{(i+1)} = \mathbf{x}^{(i)} + \frac{1}{a}\left(\mathbf{y} - \mathbf{A}\mathbf{x}^{(i)}\right), \tag{14}$$

where a is a relaxation parameter discussed further below. This is the Richardson iteration method, which for unconstrained applications has linear convergence dependent on the condition number of $\mathbf{A}$. However, constraints are enforced after every iteration, which complicates the convergence behavior. The general constraints from DAMAS-C [7] were considered with the initial exploration of this research [18]. With these, a real non-negative constraint is applied to variance terms, or terms where $(k_\xi, k_\eta) = (k_x, k_y)$,

$$\begin{aligned} \mathrm{Re}\left\{\tilde{Q}\left(k_x, k_y, k_x, k_y\right)\right\} &\geq 0 \\ \mathrm{Im}\left\{\tilde{Q}\left(k_x, k_y, k_x, k_y\right)\right\} &= 0. \end{aligned} \tag{15}$$

The quantities $\tilde{q}\left(k_x, k_y\right)$ and $\tilde{q}\left(k_\xi, k_\eta\right)$ are complex random variables. As such, when $(k_\xi, k_\eta) \neq (k_x, k_y)$ their covariance, $\tilde{Q}\left(k_x, k_y, k_\xi, k_\eta\right)$, must obey the Cauchy-Schwarz inequality from probability theory and must follow appropriate conjugate behavior,

$$\begin{aligned} \left|\tilde{Q}\left(k_x, k_y, k_\xi, k_\eta\right)\right|^2 &\leq \tilde{Q}\left(k_x, k_y, k_x, k_y\right)\tilde{Q}\left(k_\xi, k_\eta, k_\xi, k_\eta\right) \\ \tilde{Q}\left(k_x, k_y, k_\xi, k_\eta\right) &= \tilde{Q}^*\left(k_\xi, k_\eta, k_x, k_y\right). \end{aligned} \tag{16}$$

After each iteration, variance constraints are applied first to provide updated bounds for covariance constraints.

These constraints were found to be functional for the problems of interest. However, certain mixed-coherence simulations in subsequent research showed results which were extremely sensitive to grid spacing and source layout. Additionally, iteration-to-iteration solution change and residual calculations showed a high degree of irregularity for some test cases, and for these cases convergence could only be assessed by knowing the correct solution or by applying some qualitative assessment of the problem. Both issues were traced to the covariance constraint being insufficient. While it could alter the magnitude of the covariance terms, the original constraint did nothing for the phase. One potential alternative constraint set to enforce is that, when expressed as a covariance matrix, $\tilde{Q}$ must be positive semidefinite. $\tilde{Q}$ can be expressed as a covariance matrix by reshaping it from a 4-D array of size $n_{k,x} \times n_{k,y} \times n_{k,\xi} \times n_{k,\eta}$ to a 2-D array ($\mathbf{Q}$) of size $(n_{k,x} \times n_{k,y}) \times (n_{k,\xi} \times n_{k,\eta})$ with variance terms on the diagonal and covariance terms on the off-diagonal. Computationally, the ordering of the elements can be set such that this reshaping does not involve altering the memory address of any elements of $\tilde{Q}$ and the expense is minimal. This requires the ordering of x and y to match the ordering of ξ and η. After each iteration of the algorithm, the new estimate of $\mathbf{Q}$ may not be positive semidefinite, so enforcing a positive semidefinite solution after each iteration is an alternate constraint. Methods exist for finding the nearest positive semidefinite matrix, in terms of Frobenius norm, to an arbitrary matrix [19]. Straightforward MATLAB implementations of such methods exist, and one is used in this work [20]. This constraint has previously been applied to the coherent deconvolution problem, although the current positive semidefinite calculation method differs [5, 11].

Direct use of this updated constraint proved to find solutions that had a very low Frobenius norm in terms of the residual of Eq. (14). However, these solutions were in general too distributed and failed to adequately localize isolated plane waves in simple simulations. A hybrid approach, determined by testing various combinations of the old and new constraints on the cases from the initial research, was developed. For this hybrid approach, after each iteration of the solver from Eq. (14), the variance constraint from Eq. (15) is applied. The variances from this update are considered the iteration's best estimate of the source variances. The covariance matrix is then contracted to exclude zero-variance rows and columns. The nearest positive semidefinite matrix to this contracted covariance matrix is computed. This nearest positive semidefinite matrix is considered the best estimate of the coherence relationships between the various non-zero sources. It will in general have variances that differ from those determined by the variance constraint application. This output matrix is thus rescaled to recover the original variances while maintaining coherence relationships (as described further in the algorithm block), and then re-expanded to incorporate the zero-variance rows and columns from the full covariance matrix. The solution procedure is given as pseudocode in Algorithm 1.

No argument is made in this work that this method is the optimum way to solve this problem, or that the updated constraints are the most appropriate. However, note that the updated technique is applied because it properly recovers exact solutions for some test cases with simulated data and shows improved handling of some mixed-coherence test cases when compared to the previous constraint set. Perhaps more importantly, the updated constraints used in the technique appear to stabilize the iteration-to-iteration solution change and residuals sufficiently that convergence metrics can be assessed.

3.1. Linear convolution

For linear convolution, $\tilde{Q}$ must be zero-padded and $\tilde{S}$ must be constructed on the larger, padded grid scale. If this is not done, sources within the bounds of $\tilde{Q}$ may have a significant wrap-around influence on the solution procedure, depending on the particular sidelobe distribution of $\tilde{S}$. Here, the total grid size of $n_{s,x} \times n_{s,y} \times n_{s,\xi} \times n_{s,\eta}$ contains nearly 16 times the number of elements of the baseline grid, as the minimum padding for linear convolution in each dimension is $n_{s,()} = 2n_{k,()} - 1$. $\tilde{Q}$ must be padded to this size prior to transformation, and the appropriate subset of grid points selected in the $\tilde{P} - \tilde{R}$ step of the algorithm. Additional points and/or padding may be used depending on the optimum performance of a given FFT library and system memory limitations.

The increased computational burden of transforming zero-padded arrays may be partially-mitigated by exploiting the separability of the multi-dimensional FFT in conjunction with zero-padding requirements [21]. For example, if a 2-D grid of size $n_{k,x} \times n_{k,y}$ is to undergo a 2D FFT for use with linear convolution, it must

Algorithm 1: Wavenumber-frequency deconvolution algorithm

Input: $\tilde{P}$ (4-D array of size $n_{k,x} \times n_{k,y} \times n_{k,\xi} \times n_{k,\eta}$), $\tilde{S}$ (4-D array of size $n_{s,x} \times n_{s,y} \times n_{s,\xi} \times n_{s,\eta}$). See Section 3.1 for sizing of $\tilde{S}$. Specification of the discretization of the wavenumber domain is discussed in Section 3.5. $\tilde{S}$ should be shifted such that the element corresponding to $k_x = k_y = k_\xi = k_\eta = 0$ is the first element of the array for proper FFT-based convolution.

Output: $\tilde{Q}$ (4-D array of size $n_{k,x} \times n_{k,y} \times n_{k,\xi} \times n_{k,\eta}$). The discretization and range of the wavenumber domain in $\tilde{Q}$ matches that in $\tilde{P}$. Note that as the system of equations to be solved is ill-conditioned and the equivalent $\mathbf{A}$ associated with $\tilde{S}$ usually rank-deficient, $\tilde{Q}$ is not expected to be unique. It is simply a constrained solution which attempts to minimize the residual u given in Eq. (26).

begin

- Forward transform $\tilde{S}$ with a 4-D Fourier transform, $\hat{S} = \mathrm{FFT4}\left[\tilde{S}\right]$.
- Compute $a = \frac{\lambda_{\mathbf{A},max}}{2} + \epsilon$, where ϵ is a small value to ensure $a > \frac{\lambda_{\mathbf{A},max}}{2}$. See Section 3.2.
- Initialize all elements of solution array, $\tilde{Q}^{(0)} = 0$.
- Initialize normalized residual and solution change, $u^{(0)} = v^{(0)} = 1$, as defined in Section 3.3.
- **while** Convergence criterion involving u and/or v is unmet (see simulated data discussion)
  - Forward transform $\tilde{Q}^{(i)}$, $\hat{Q}^{(i)} = \mathrm{FFT4}\left[\tilde{Q}^{(i)}\right]$. Follow the zero-padding requirements addressed in Section 3.1 to ensure linear convolution.
  - Compute the element-wise product of arrays $\hat{S}$ and $\hat{Q}^{(i)}$, $\hat{R}^{(i)} = \hat{S} \cdot \hat{Q}^{(i)}$.
  - Inverse transform $\hat{R}^{(i)}$ to $\tilde{R}^{(i)}$, $\tilde{R}^{(i)} = \mathrm{IFFT4}\left[\hat{R}^{(i)}\right]$. Discard the padded elements of $\tilde{R}^{(i)}$.
  - Update the solution estimate, $\tilde{Q}^{(i+1)} = \frac{1}{a}\left(\tilde{P} - \tilde{R}^{(i)}\right)$.
  - Reshape $\tilde{Q}^{(i+1)}$ to $\mathbf{Q}^{(i+1)}$.
  - Enforce positivity on the diagonal of $\mathbf{Q}^{(i+1)}$ by setting negative values to zero.
  - Contract $\mathbf{Q}^{(i+1)}$ by deleting rows and columns with zero variance on the diagonal.
  - Store the diagonal of $\mathbf{Q}^{(i+1)}$.
  - Update $\mathbf{Q}_{psd}^{(i+1)}$ as the nearest positive semidefinite matrix to $\mathbf{Q}^{(i+1)}$.
  - Re-scale $\mathbf{Q}_{psd}^{(i+1)}$ based on the diagonal of $\mathbf{Q}^{(i+1)}$. This is done by multiplying the matrix elements by the ratio of the products of the appropriate square roots of the diagonal elements before and after the positive semidefinite calculation. For example, $\mathbf{Q}_{psd}^{(i+1)}(I,J) = \mathbf{Q}_{psd}^{(i+1)}(I,J) \times \sqrt{\mathbf{Q}^{(i+1)}(I,I) \times \mathbf{Q}^{(i+1)}(J,J)} / \sqrt{\mathbf{Q}_{psd}^{(i+1)}(I,I) \times \mathbf{Q}_{psd}^{(i+1)}(J,J)}$.
  - Expand $\mathbf{Q}_{psd}^{(i+1)}$ to the original size of $\mathbf{Q}^{(i+1)}$ by adding rows and columns of zeros at the appropriate indices deleted in the contraction process.
  - Reshape $\mathbf{Q}_{psd}^{(i+1)}$ to $\tilde{Q}^{(i+1)}$. Compute $u^{(i)}$ from Eq. (26) and $v^{(i)}$ from Eq. (27).

be zero-padded to a grid of size $n_{s,x} \times n_{s,y}$, which has nearly four times as many elements. However, the 2-D transform can be decomposed into a 1-D FFT operating on the first dimension, followed by a 1-D FFT operating on the second dimension. When the first of the FFTs operates on the padded $n_{s,x} \times n_{s,y}$ grid, half of the grid has all zeros in the transform dimension, and thus both the input and output are zero. The 1-D FFT can be skipped on these grid points, so only $n_{k,y}$ 1-D FFTs of length $n_{s,x}$ are performed on the first dimension. The second dimension still requires $n_{s,x}$ 1-D FFTs of length $n_{s,y}$. This computation scheme can be extended to 4-dimensional padded transforms and shows significant reduction in computational overhead.

3.2. Relaxation parameter

The relaxation parameter a is a critical component of the algorithm as the iterative update diverges without it. With DAMAS2 as an example fast-convolution technique, this parameter is specified as the sum of the absolute value of the 2-D array response within the baseline grid domain. Extended to this 4-D problem, it is computed by

$$a = \sum_{k_x=k_{min,x}}^{k_{max,x}} \sum_{k_y=k_{min,y}}^{k_{max,y}} \sum_{k_\xi=k_{min,\xi}}^{k_{max,\xi}} \sum_{k_\eta=k_{min,\eta}}^{k_{max,\eta}} \left| \tilde{S}\left(k_x, k_y, k_\xi, k_\eta\right) \right|. \tag{17}$$

This value is effectively the maximum column sum of absolute values of the $\mathbf{A}$ representation of $\tilde{S}$ in Eq. (14), which corresponds to the matrix norm $||\mathbf{A}||_1 = \max\limits_J \sum_{I=1}^{(n_{k,x} \times n_{k,y})^2} |\mathbf{A}(I,J)|$ [22]. As the spectral radius of a square matrix r_σ must be less than or equal to its operator norms, using this norm as a relaxation parameter is a conservative way to stabilize the solution procedure. It should be noted that stabilization does not guarantee convergence, as seen with simulated data in subsequent sections.

A smaller value of a which leads to larger solution steps and maintains stability may be derived, following the method presented by Atkinson [22]. Eq. (1) can be restructured by splitting $\mathbf{A}$,

$$\mathbf{A} = \mathbf{B} - \mathbf{C}, \tag{18}$$

and rewriting Eq. (1) as

$$\mathbf{Bx} = \mathbf{y} + \mathbf{Cx}. \tag{19}$$

The iterative method is thus given as

$$\mathbf{Bx}^{(i+1)} = \mathbf{y} + \mathbf{Cx}^{(i)}. \tag{20}$$

Matrix $\mathbf{D}$ can be defined as

$$\mathbf{D} = \mathbf{B}^{-1}\mathbf{C}. \tag{21}$$

The stability criterion for the (unconstrained) iteration method is then given as

$$r_\sigma\left(\mathbf{D}\right) < 1. \tag{22}$$

With some rearrangement, Eq. (14) yields $\mathbf{B} = a\mathbf{I}$ and $\mathbf{C} = a\mathbf{I} - \mathbf{A}$. This gives $\mathbf{D} = \mathbf{I} - \frac{1}{a}\mathbf{A}$. As the eigenvalues of the identity matrix are unity and all vectors are its eigenvectors, this yields

$$\lambda_{\mathbf{D}} = 1 - \frac{\lambda_{\mathbf{A}}}{a}. \tag{23}$$

Since $r_\sigma(\mathbf{D})$ is the magnitude of the largest eigenvalue of $\mathbf{D}$,

$$|\lambda_{\mathbf{D}}|_{max} = \left|1 - \frac{\lambda_{\mathbf{A}}}{a}\right|_{max} < 1. \tag{24}$$

For this to hold, $\mathbf{A}$ must be positive semidefinite and

$$\frac{\lambda_{\mathbf{A},max}}{2} < a, \tag{25}$$

so the minimum relaxation parameter is simply half of the spectral radius, or largest eigenvalue, of $\mathbf{A}$. Note that there is no expectation that $\mathbf{A}$ must be positive semidefinite. In the authors' experience, the matrix was always positive semidefinite when diagonal removal was not applied to the data. Diagonal removal was found to lead to $\mathbf{A}$ having negative eigenvalues for certain combinations of grid spans and densities. In these circumstances, testing verified that no value of a prevented the solution procedure from diverging. As such, the grid range and density was modified until the resultant $\mathbf{A}$ was positive semidefinite.

This relaxation parameter calculation may appear problematic at first as the goal of this method is to avoid computing and storing matrices of size $\mathbf{A}$. However, there are methods such as the implicitly-restarted Arnoldi Method [23] for computing the largest eigenvalue of $\mathbf{A}$ using a function call which evaluates the matrix vector product $\mathbf{Ax}$ for a given input vector $\mathbf{x}$, rather than using $\mathbf{A}$ itself. The value of a computed by this method for the problems considered in this study is often orders of magnitude smaller than that given by Eq. (17) for the modeled arrays and grids. With this value the solution method is stable for the cases considered. When $\mathbf{A}$ is no longer positive semidefinite, the technique will diverge and the wavenumber extent and resolution of the grid should be reconsidered. To re-iterate, this is the stability criterion for the unconstrained formulation of Eq. (14), and does not account for the positive variance and positive semidefinite constraints applied to $\mathbf{Q}$.

3.3. Residuals and precision

Two quantities are tracked and stored for every iteration in this work. The first is the residual or relative error between the source estimate convolved with the array response and the wavenumber-transformed array data. This is expressed as the ratio of ℓ^2 vector norms,

$$u^{(i)} = \frac{\left|\left|\tilde{P} - \tilde{R}^{(i)}\right|\right|_2}{\left|\left|\tilde{P}\right|\right|_2}, \tag{26}$$

where the arrays $\tilde{P}$ and $\tilde{R}^{(i)}$ are reshaped to column vectors for the calculation. The second is the scaled change in solution from one iteration to the next, expressed as the ratio of ℓ^1 vector norms,

$$v^{(i)} = \frac{a \left|\left|\tilde{Q}^{(i+1)} - \tilde{Q}^{(i)}\right|\right|_1}{\left|\left|\tilde{P}\right|\right|_1}. \tag{27}$$

Both quantities are scaled such that, neglecting the application of constraints, they are unity for $i = 0$. This is done with v by including the relaxation parameter a in the numerator. The behavior of each is considered on a case-by-case basis with simulated data in an attempt to determine convergence criteria.

In the initial version of this work, it was determined that single-precision floating point analysis was sufficient for data analysis. Subsequent analysis showed that this was generally the case with the initially-selected constraints. However, the calculation of the nearest positive semidefinite matrix involves matrix decompositions which show more sensitivity to the precision of the calculations. While some test cases still performed as expected with the updated constraints for single-precision analysis, convergence became more difficult to track with others. As such, it is recommended that this algorithm be used with double-precision analysis whenever possible, and all presented results are computed using double-precision.

3.4. Additional topics from preliminary work

Two topics from the preliminary version of this work are not included in the current discussion [18]. The first of these was a multiscale approach to determine an improved estimate of $\tilde{Q}^{(0)}$. The multiscale approach involved constructing low-resolution grids with large $\Delta k_{()}$ values, solving for $\tilde{Q}^{(0)}$ on these grids, and then upscaling the results to a more refined grid. This upscaling approach showed promise with specific problems, but the results were highly-dependent on the interpolation scheme used and the particular problem of interest. No general approach was determined in subsequent research, and so the method is excluded from the current report.

The second topic was a wavenumber-domain integration technique used in an attempt to more accurately capture the effects of sources located between grid points. Upon further simplification, this technique reduced to applying a sinc-function window to the microphone array data, weighted by both the spatial and conjugate-spatial dimensions. Subsequent investigation showed the benefits of this particular weighting to be questionable at best. While spatial weighting of microphone array data is common in aeroacoustic analysis [24], sinc functions are rarely used and investigation of an optimum spatial window is beyond the scope of this work.

3.5. Comments on scaling

The computational savings of this algorithm in terms of floating point operations is significant. For the matrix-vector multiply solution of Eq. (14), each forward multiplication of $\mathbf{A}$ (assuming $n_{k,x} = n_{k,y}$) has computational complexity of $O(n_{k,x}^8)$. Conversely, the Fourier transform convolution has a computational complexity of $O(n_{k,x}^4 \log n_{k,x})$, where the specifics of the scaling are partially-dependent on the zero-padding scheme used in Section 3.1. The application of the positive semidefinite constraint involves a singular value decomposition of the matrix form of $\tilde{Q}$ which has a complexity of $O(n_{k,x}^6)$. This becomes the most expensive part of the algorithm in terms of scaling. However, it is partially mitigated by the contraction process where only non-zero variance rows and columns of the covariance matrix are retained.

Memory scaling must also be considered. While this algorithm bypasses explicit storage of $\mathbf{A}$, which would have a size of $(n_{k,x} \times n_{k,y} \times n_{k,\xi} \times n_{k,\eta})^2$, problem size can still be an issue. Specifically, the scaling associated with 4-D data and zero-padding is non-trivial. As an example, consider the case of a square grid where $n_{k,()} = 25$, empty parentheses meaning the grid assignment applies to all dimensions. Each array must be padded to $n_{s,()} = 49$ and each contains 5.76 million elements. While this has moderate storage requirements, 92.2 MB for double-precision complex, it is still a significant amount of data to handle with an algorithm which may require many iterations. Hardware-tuned FFT algorithms [25] can help mitigate this expense, but the cost of a given problem size is still a driving concern.

Previous research [1] indicates that in deconvolution the grid spacing should be between approximately 5% and 20% of the sampling pattern's 3-dB main lobe width. In the wavenumber-frequency domain, this sets an effective maximum value for $\Delta k_{()}$ for a given array. The wavenumber bounds of interest are highly problem-dependent. In the case of plane waves arriving from a limited cone of directions, $k_{min,()}$ and $k_{max,()}$ can simply be selected to properly encompass the appropriate region within the wavenumber-frequency domain. However, for a general problem in a quiescent medium where no information is known about the acoustic field, the bounds will need to meet the acoustic wavenumber, $2\pi f/c_0$ (rad/m) or f/c_0 (m^{-1}) to encapsulate every potential direction of arrival. Convection effects would offset this region, demanding that the modified acoustic radiation ellipse be encompassed instead. Extending $k_{min,()}$ and $k_{max,()}$ beyond the acoustic wavenumber to evaluate subsonic hydrodynamic contamination also extends the grid size.

These requirements, combined with the aforementioned scaling issue, may currently limit the method's usage to either problems with limited direction of arrival or low frequencies, depending on an array's main lobe width. For example, the 0.74 m aperture outer array used at the University of Florida Aeroacoustic Flow Facility (UFAFF) [26] has a 3-dB main lobe width of 1.47 m^{-1} in the wavenumber domain. This is computed by evaluating the wavenumber transform of the microphone locations to generate the array's wavenumber response on a high-resolution wavenumber grid. The lobe width is extracted from this grid. The array can adequately capture the entire acoustic radiation circle with a $\Delta k_{()}$ of 20% of the sampling pattern's 3-dB main lobe width at $f = 1$ kHz and $c_0 = 343$ m/s with $n_{k,()} = 21$. An individual transform of a grid required for this scale is reasonably quick, and thus can be considered for analysis. Higher frequencies can become an issue, as acoustic wavenumber scales linearly with frequency. To maintain a given $\Delta k_{()}$, this means that $n_{k,()}$ must also scale linearly with frequency, so the overall problem scales as the fourth power of frequency. Under some circumstances in this work, the spacing recommendation is relaxed to spacings up to 50% of the 3-dB width to allow more rapid assessment of simple cases. The most refined grids have spacings of 25% of the 3-dB width.

4. Application

Usage of the deconvolution technique is now presented. A detailed study using simulated data has been conducted. The majority of these results are presented in Appendix A. Key discussion points from the appendix are:

1. accounting for coherence in the deconvolution process adds unnecessary computational burden for incoherent problems,
2. diagonal removal improves the convergence rate of the method for this array layout and the selected grids of interest,
3. accounting for coherence in the deconvolution process can extract the correct magnitude, phase, and coherence relationship of partially-coherent plane waves,
4. a reasonable convergence metric is a two order-of-magnitude reduction in v after it begins exhibiting a power law relationship with u,
5. offsetting ideal plane waves between wavenumber grid points can lead to a situation with no feasible convergence behavior,
6. isolated point sources show reasonable behavior with deconvolution whether or not coherence is allowed in the processing,
7. determining the solid angle of the source observed by the array provides a reasonable boundary for source level integration, and
8. accounting for coherence in the deconvolution process and using the defined integration boundary can extract good estimates of individual levels, coherence, and phase relationships between ideally-coherent point sources (a synthetic data set representing a source and its image).

Two more applications are treated in the main body of this work. Both are considered representative of aeroacoustic wind tunnel measurements. The first is a simulated data set representing a source and its image in a subsonic flow, contaminated by a strong turbulent boundary layer. Array data analysis in the wavenumber-frequency domain has potential use in closed-walled wind tunnel test sections with flow [27], so such a simulation is of interest. The second is a real data set from an open-jet wind tunnel test in which trailing edge noise was measured as generated by a NACA 0012 airfoil. Both data sets use the microphone layout of the outer UFAFF array [26] mentioned in Section 3.5. As stated there, the array has a 3-dB beamwidth in the wavenumber domain of $w = 1.47$ m^{-1}. Both data sets are evaluated at a temporal frequency of $f = 2$ kHz.

4.1. Simulated data: point source with a reflection in flow

A mean flow of Mach number $M = 0.3$ is modeled as passing over the array face in the negative x-direction. The source and its image are treated as displacement point sources in a uniform mean flow [28]. The source strength is scaled to have a true level of 100 dB at the array center. The image level at the array center is 97.0 dB. The sum level at the array center is 102.8 dB, as the phase angle between the image and source is 72.8° with the in-flow source and propagation models.

The Corcos boundary layer cross-spectrum is selected for the turbulent boundary layer model [29]. Based on existing work the eddy convection velocity is chosen to be 63% of the free-stream Mach number for 2 kHz [27], with the appropriate coefficients from the Corcos decaying exponentials determined from this choice. The boundary layer fluctuations are simulated to have a level of 120 dB on the array face, so the acoustic measurement is modeled as experiencing contamination from hydrodynamic pressure fluctuations nearly an order of magnitude greater than the acoustic signal. A separate CSM of the Corcos boundary layer is generated and summed with the acoustic source and image CSM, so the hydrodynamic data are modeled as perfectly incoherent with the acoustic data. The resultant variance as a function of wavenumber is shown in Fig. 1. The Corcos boundary layer manifests as the strong structure in the extreme negative k_x portion of the plot. For the selected transform sign convention, waves travel in the direction of the sign of their wavenumber vector components.

The transform grid for this case is sized to $n_{k,x} = 116$ and $n_{k,y} = 37$, with $n_{s,x} = 231$ and $n_{s,y} = 75$. The resultant relaxation parameter is $a = 1.10 \times 10^4$. This sizing captures the full acoustic radiation region, as well as the energetic regime of the Corcos boundary layer model. The acoustic radiation boundary is plotted as in Appendix A. The boundary is calculated using the method described in Appendix C. The plot shows that a wavenumber transform of the data successfully separates hydrodynamic fluctuations from acoustic signals, even when the boundary layer fluctuations are significantly stronger than the acoustic signals. However, it appears sidelobes of the Corcos boundary layer are present in the acoustic region and overlay the acoustic signals. The reader is reminded that diagonal removal is applied in this procedure, so all of the turbulent boundary layer contamination in the wavenumber domain occurs due to the correlation of boundary layer fluctuations between pairs of microphones.

Deconvolution results using both the proposed coherent method and incoherent equivalent are shown in Fig. 2. As discussed in more detail in Appendix A, the incoherent equivalent neglects covariance between wavenumbers and only applies the positivity constraint. This is similar to a more conventional deconvolution scheme. Convergence of the coherent method occurs after approximately 4.61×10^3 iterations. Here, v drops below 10^{-13} with a corresponding value of $u = 1.10 \times 10^{-12}$ in Fig. 3a. The incoherent method has more difficulty with this particular case, taking 50 million iterations to approach a value of $v = 3.18 \times 10^{-16}$. The corresponding u for the incoherent method is 3.08×10^{-2}. The source distributions appear similar, though not identical to, those for the source and image deconvolution without flow shown in Appendix A. The

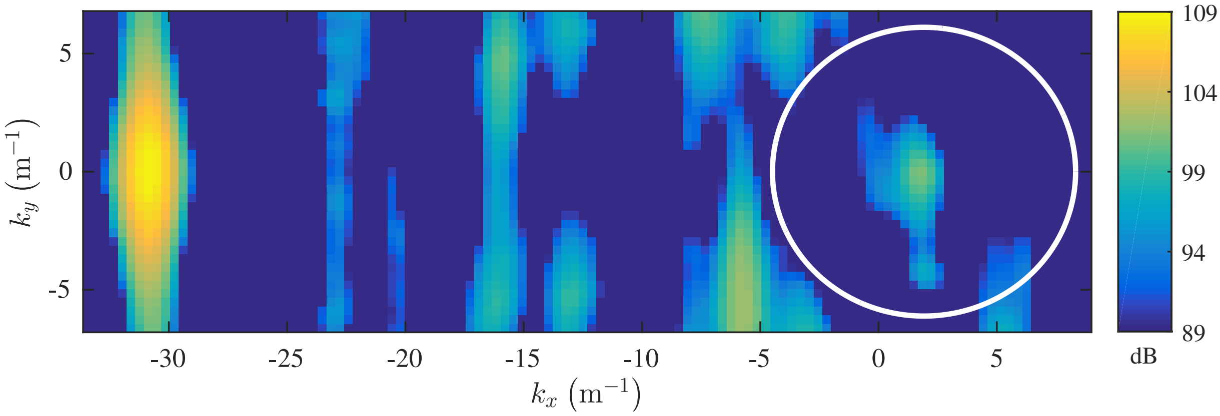

Figure 1. Transform variance of the simulation of the point source with reflection combination in-flow, $M = 0.3$ in the negative x-direction.

coherent method appears to preserve the overall shape of the source and image wavenumber distributions, although some structure of the source region manifests outside of the integration bounds. The acoustic region of the incoherent method appears similar to that of the incoherent method without flow. The hydrodynamic region, however, appears as a large set of discrete waves as opposed to the continuous distribution expected from the model. The coherent method maintains the expected continuous distribution.

The integration metrics for this case are the same as those used for the deconvolution of the source and image simulation without flow from Appendix A. Levels are plotted as a function of solution change in Fig. 3b. The source level converges to 94.6 dB, over 5 dB below the true level of 100 dB at the array center. The image level converges to 92.3 dB, nearly 5 dB below the true level of 97.0 dB at the array center. The combined level is calculated as 97.1 dB, over 5 dB below the array center level of 102.8 dB. The overall agreement with the array center microphone is significantly worse for this case than seen with the no-flow simulation. Visually the integration bounds still appear to fully-encapsulate the source and image regions, so level underprediction does not appear to be due to boundary definition problems. The poor signal-to-noise ratio between the acoustic and hydrodynamic signals appears to drive the deconvolution process towards a low residual solution with underpredicted acoustic levels. This is reinforced when evaluating the coherence-squared function between the sources in Fig. 3c. The coherence-squared should be unity. Instead it reaches a final value of 0.26. Significant amounts of power incoherent between the acoustic source and its image are present in the source and image regions. Interestingly, the phase relationship plotted in Fig. 3d recovers a phase angle of 74.6°, which is close to the array center value of 72.8°. While the levels of coherent power between the source and image are incorrect, the calculated phase relationship between the sources still appears to track well with the array center phase relationship. It should be noted, however, that direct calculation of coherence-squared and phase angle from the pre-deconvolution transform data (without

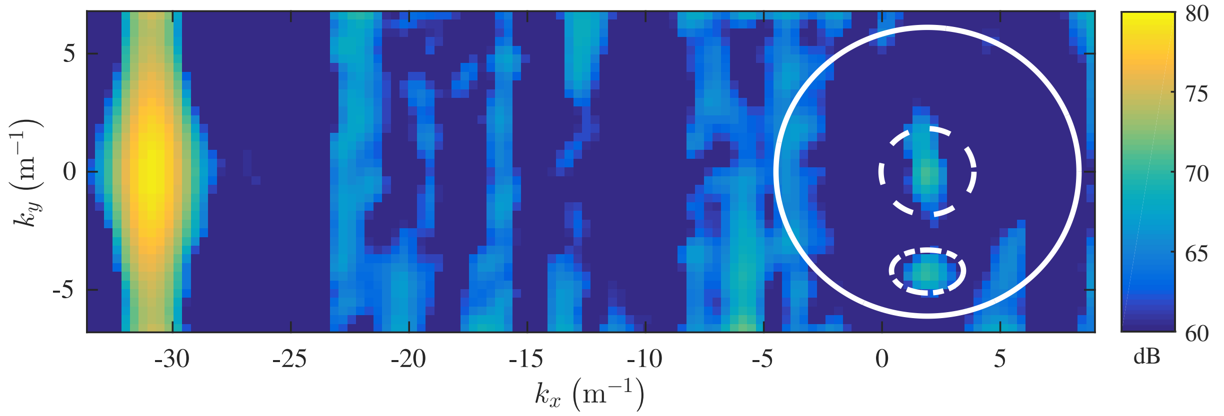

(a) coherent deconvolution

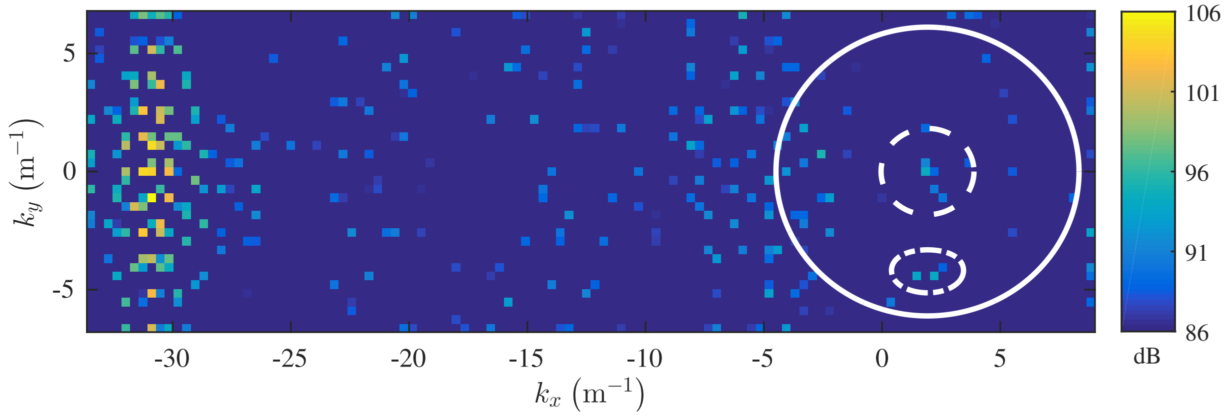

(b) incoherent deconvolution

Figure 2. Variances from deconvolution of point source with reflection in-flow using $\Delta k_{()} = w/4$ spacing grid for both coherent and incoherent methods.

diagonal removal) yields $\gamma^2 = 0.18$ and $70.2°$, so the overall change from naive estimates for these quantities is small. As with the simulated data sets in Appendix A, integrated quantities appear converged when v has reduced by two orders of magnitude after beginning a power law relationship with u. This occurs at $v = 10^{-6}$.

Integrated metrics for the incoherent solution are also computed (though not plotted). The source level is 99.2 dB. The image level is 98.1 dB. The combined level is 101.7 dB. All of these values are significantly closer to the array center values than the coherent deconvolution equivalents. The combined level likely performs well because the array center phase angle of $72.8°$ is close to $90°$, where powers can be added directly without covariance information. There is insufficient information to determine why the individual source levels are closer for incoherent deconvolution than coherent deconvolution.

The coherence relationship between sources is further considered in Fig. 4. Here, the coherence-squared value of each grid point referenced to the closest grid point to the wavenumber corresponding to the wave propagating from the source to the array center microphone, $k_x = 1.84$ m^{-1}, is plotted. As shown, there is noticeable coherence between the source and the center of the turbulent boundary layer wavenumber distribution near $k_x = -31$ m^{-1}. Based on the simulation inputs (as well as the process for generating them), this is non-physical.

For this simulation and many experiments, it may be safe to assume that significant wavenumber power outside of the acoustic radiation boundary is statistically independent from that within the radiation boundary. Here, the turbulent boundary layer passing over the array face can be assumed to have no correlation with the acoustic sources of interest. When this is the case, a zoning procedure similar to that used in DAMAS-C can be implemented [7]. For such a procedure the covariance between grid points inside the acoustic radiation boundary and those outside the boundary is set to zero during the constraint application phase of each iteration. This modified method is implemented and analyzed. Convergence occurs in just over 5.51×10^3 iterations, with v dropping below 10^{-13} and a corresponding u of 1.59×10^{-12}. The computed source and image values do show improved agreement with the array center data, with a source level of 98.6 dB, image level of 95.5 dB, and combined level of 100.6 dB. However, the coherence estimate is only slightly better with $\gamma^2 = 0.31$. The phase estimate is in worse comparison with the array center phase, with the computed relative angle at $81.9°$. It appears that enforcement of an additional constraint provides questionable added value (trading source levels for phase angle) in this case. Even for simulations, extracting quantitative acoustic data in the presence of strong contamination may be difficult.

4.2. Experimental data: trailing edge noise

This case is taken from an existing trailing edge noise data set collected in UFAFF [30]. While trailing edge noise data are not expected to have strong coherent features which require this algorithm, such a test case allows validation of the method as it ought to recover a reasonable solution. Some assessment of

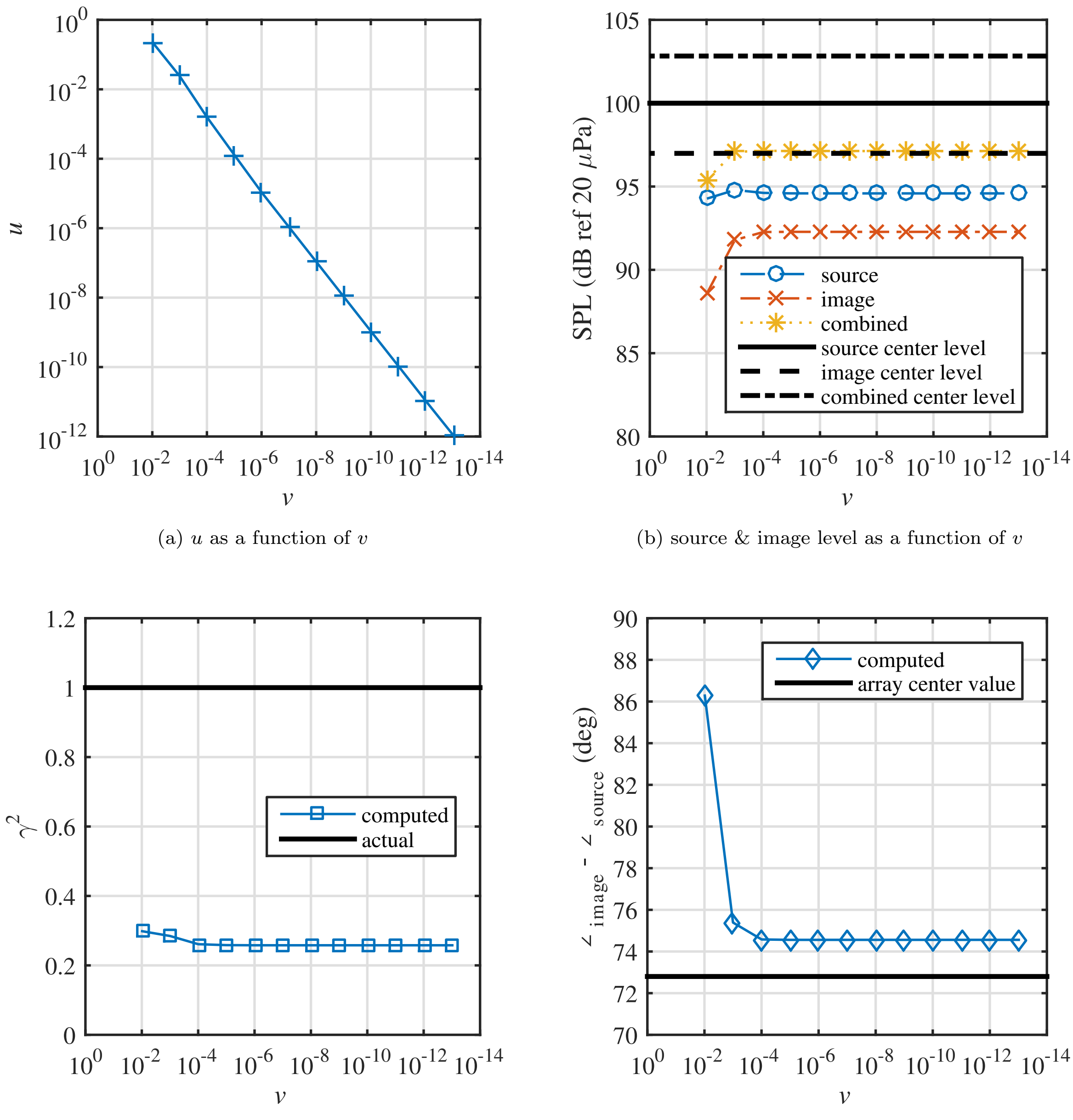

(a) u as a function of v

(b) source & image level as a function of v

(c) γ^2 between image and source

(d) Phase angle between image and source

Figure 3. Convergence behavior and metrics evaluation of the coherent solution technique for the point source with reflection in-flow.

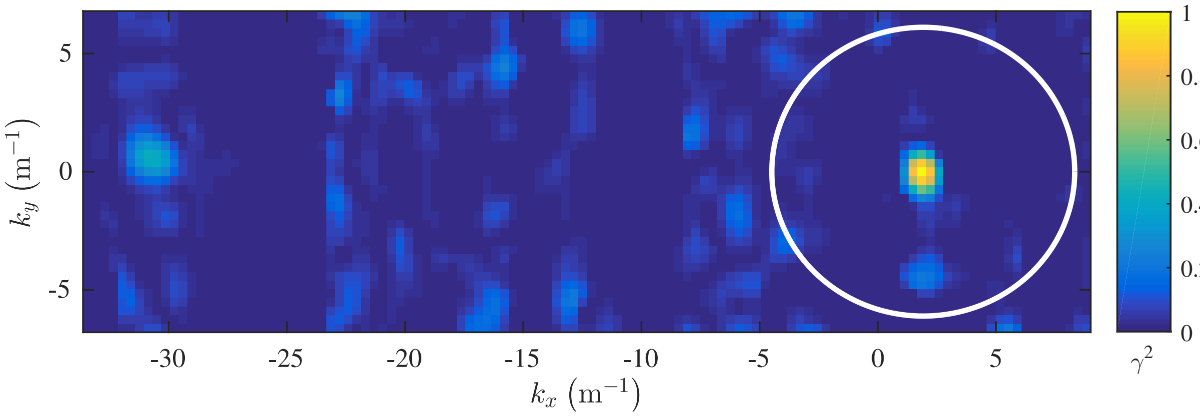

Figure 4. Coherence-squared between the wavenumber bin approximately corresponding to propagation from the source to array center, $(k_x, k_y) = (1.84, 0)$ m^{-1}, and the total deconvolution domain for the point source with reflection in-flow.

wavenumber field coherence is also possible.

Data are acquired for a 0.3048 m chord, 0.74 m span NACA 0012 airfoil, in this case at a Mach number of $M = 0.17$ in the negative x-direction, as the x-direction of the array coordinate system points upstream. Additional details of the experiment can be found in the reference. A photograph of the installation is shown in Fig. 5, while a legend of the illustrations used in the baseline beam map at $z = 1.13$ m is shown in Fig. 6. Here, flow is from right to left. The airfoil trailing edge center span is located at (0,0,1.13) m from the array center. A conventional beam map of the array data at 2 kHz, using Amiet's shear layer correction method [31], is shown in Fig. 7. The beam map has a 10 dB dynamic range in the plot as opposed to the 20 dB used throughout the rest of this work. Little appreciable flow is noticeable over the array face, as the facility is an open-jet wind tunnel and the array is located outside of the flow. Microphone cross-correlations are evaluated for any potential hydrodynamic time scales, and none are observed. As a final check, a large-scale incoherent transform of the data in the wavenumber domain is evaluated. No appreciable hydrodynamic fluctuations are observed.

The variance of the wavenumber transform of the data is plotted in Fig. 8. As with the beam map, experimental data are plotted on a 10 dB scale. The main trailing edge noise source is seen in the central region of the acoustic radiation boundary. A secondary source at the extreme positive k_x of the acoustic radiation region is at an angle corresponding to a signal arriving from the facility's open-jet shear layer impinging on the jet collector. As mentioned previously, the transform convention used in this work means a wave manifesting with a positive k_x wavenumber indicates it is traveling in the positive-x direction. The impingement line is significantly out-of-plane from the beam map in Fig. 7, so the beam map x-bounds would have to be expanded to capture any beamforming artifacts from this secondary source.

The wavenumber grid has size $n_{k,x} = 41$ points and $n_{k,y} = 43$ points, with the convolution grid sized to

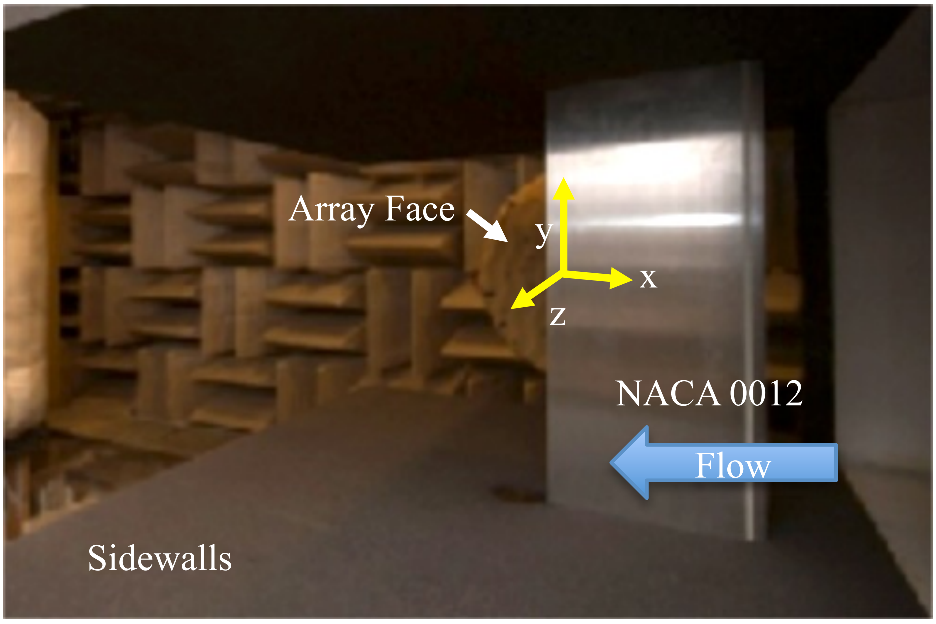

Figure 5. NACA 0012 trailing edge noise measurement installation.

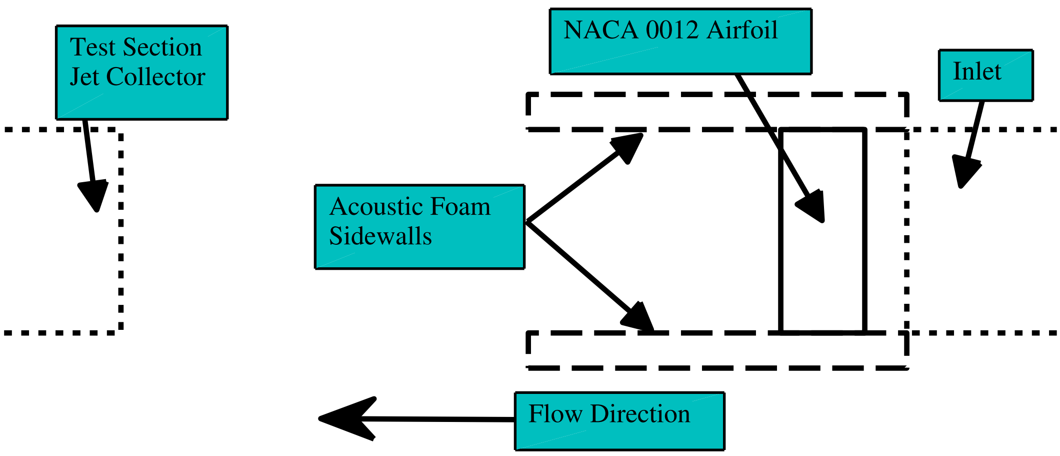

Figure 6. Legend of facility schematic used in the beam map.

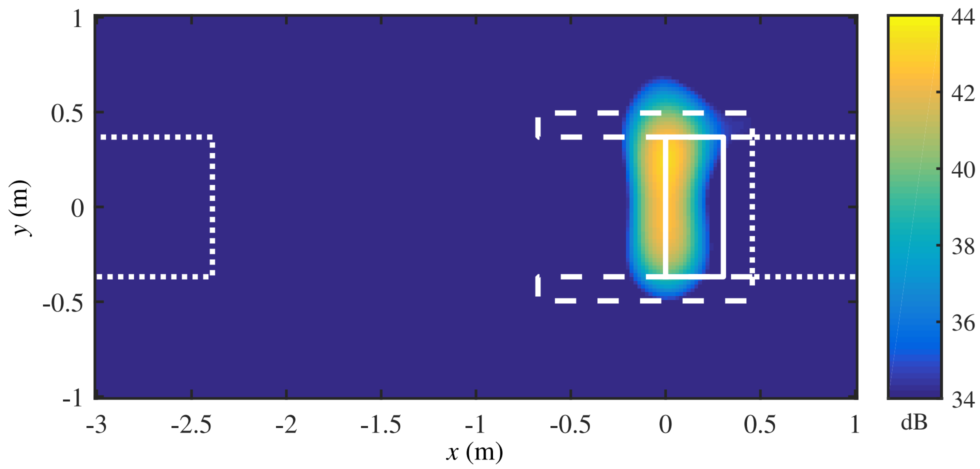

Figure 7. Baseline beamforming for NACA 0012 trailing edge noise experiment at 2 kHz, $z = 1.13$ m.

$n_{s,x} = 81$ points and $n_{s,y} = 85$ points and the grid density set to $\Delta k_{()} = w/4$. The corresponding relaxation parameter is $a = 2.89 \times 10^3$. Note that this grid is sized well beyond the acoustic radiation domain in the negative-k_x and positive-k_y directions. This sizing was determined using trial-by-error after the initial grid from the simulated point source case failed to converge in the sense that u never reduced below 10^{-1} for increasing iteration count and decreasing v (no power law reduction relationship was observed). It was found that energetic sidelobe structures lying on the deconvolution boundary would manifest as strong false sources in the deconvolution procedure. Improvement in u was only achieved once the boundary was expanded such that the majority of each of these sidelobe structures did not lay on or just outside of the deconvolution boundary. While such a grid sizing rule may not be possible for every deconvolution application, it may provide some guidance in handling analyses which show difficulty converging in terms of u and manifest strong boundary sources.

Deconvolution results are shown in Fig. 9. Convergence occurs in just over 19.9×10^3 iterations, with v dropping below 10^{-12} and $u = 2.21 \times 10^{-11}$ for the solution shown in Fig. 9a. The incoherent method takes significantly more iterations, nearly 600,000, before v drops below 10^{-12}. The value of u reaches a steady value of 2.03×10^{-1} far before this. As in other cases, the coherent method tends to show distributions of energy whereas the incoherent method isolates discrete plane waves. Both methods show the trailing edge noise source region and the shear layer impingement source. However, the coherent method shows additional source regions. If they are not simply deconvolution artifacts, these lower-level sources would correspond to some boundary layer noise from the porous sidewalls in the case of the regions offset in the k_y direction, and some noise arriving from the test section inlet in the case of the region at $k_x = -3.5$ m^{-1}. The angle projection would suggest noise propagating from within the inlet rather than sources located on its edges

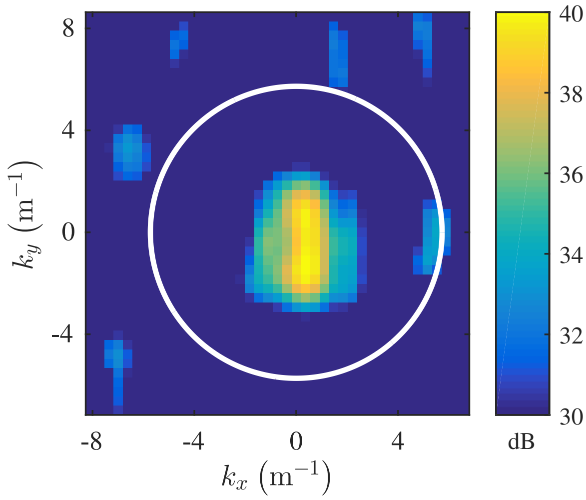

Figure 8. Transform variance of the NACA 0012 trailing edge noise experiment 2 kHz data.

due to flow interaction. However, insufficient data are available to draw any serious conclusions regarding this potential source.

Integration bounds are again computed and plotted. As mentioned in Appendix A, the method of handling well-separated discrete point sources in prior cases will not work when sources are close enough that the computed wavenumber domains overlap. For this case, the trailing edge is modeled as a dense line of point sources. The acoustic propagation path from each of these point sources to the outer ring of the array is traced using Amiet's method [31] and the resultant wavenumber bounds of each source computed using the wave angles at the outer ring. The union of the wavenumber bounds for all of the modeled sources is computed, and the boundary of this union region with the selected grid density expansion (see Appendix B) is used in the calculation of Ψ. As shown the bounds accurately capture the source region. As with other cases, this methodology generates bounds which appear conservative, leading to integrated levels which adequately capture levels but may impede source isolation.

The convergence behavior for the algorithm evaluating u as a function of v is plotted in Fig. 10a. The level, computed from the aforementioned Ψ, as a function of v for the coherent deconvolution method is plotted in Fig. 10b. As with many of the cases in Appendix A, v reaches a value of 10^{-6} near where it experiences two orders of magnitude reduction after establishing a power law relationship with u. At this value, the computed level is converged to a value of 47.7 dB. This is compared to the best estimate of the trailing edge noise at the array face from the reference. The value is computed by the two-microphone dipole method and has a value of 48.0 dB. The uncertainty bounds of the two-microphone dipole method, [47.5 48.3] dB, are sufficiently wide that the deconvolution result is nominally within agreement. The incoherent deconvolution technique results in an integrated level of 48.0 dB, also in agreement with the

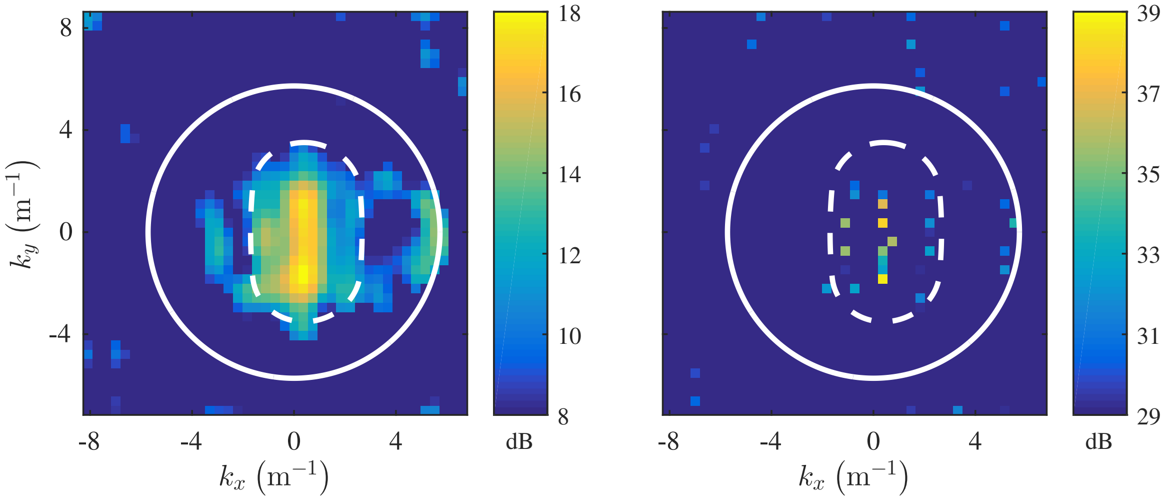

(a) coherent deconvolution

(b) incoherent deconvolution

Figure 9. Variances from deconvolution of 2 kHz trailing edge noise data, $\Delta k_{()} = w/4$.

nominal two-microphone dipole method. As with many cases studied in Appendix A, while the incoherent analysis generates variance distributions which appear intuitively less sensible, it does compute reasonable integrated levels.

The coherent deconvolution technique provides the ability to assess statistical relationships between wavenumber vectors. An example of the utility of such analysis for an airframe noise experiment is now given with a qualitative assessment of the coherence-squared function's behavior. The coherence-squared function referenced to the wavenumber approximately going from the center of the array to the center of the model trailing edge, $(k_x, k_y) = (0.37, 0)$ m^{-1}, is shown in Fig. 11a. The trailing edge noise source shows little distributed coherence. However, one noticeable feature is that it appears to maintain coherence further in the streamwise k_x direction than in the spanwise k_y direction. This is emphasized in Fig. 11b where slices of the map in Fig. 11a which pass through $(k_x, k_y) = (0.37, 0)$ m^{-1} are plotted. The width of the high-coherence region is greater for the k_y = constant k_x data than for the k_x = constant k_y data. While there is insufficient evidence to accept the quantitative levels of the plotted coherence behavior as describing the structure of the trailing edge noise source coherence, the relationship between streamwise and spanwise coherence is well known and documented [32]. Even at this level of a rudimentary analysis, some assessment of the qualitative features of the acoustic field's coherence is possible.

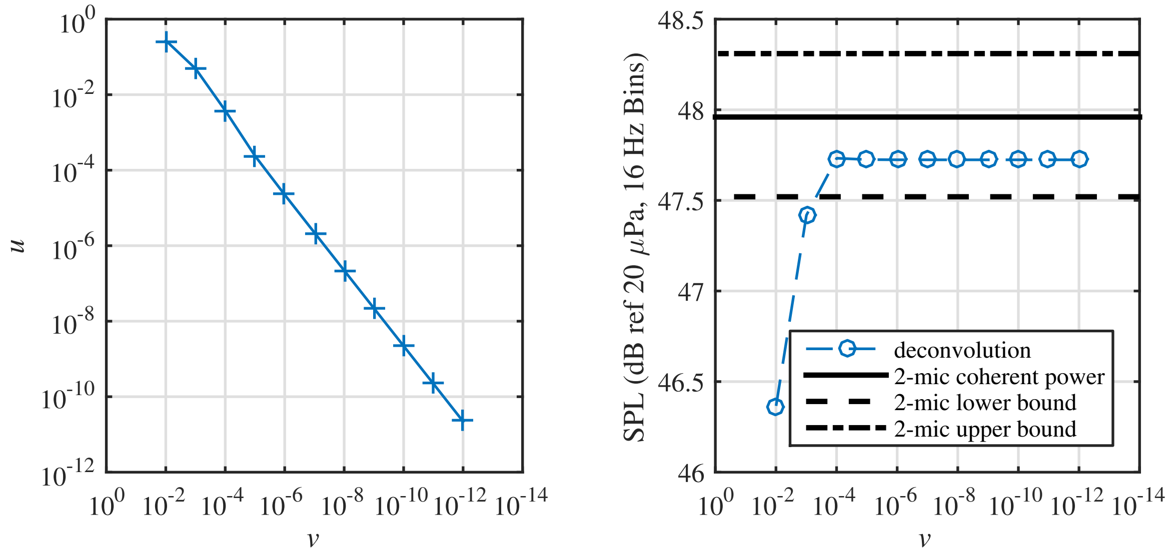

(a) u as a function of v

(b) Level as a function of v

Figure 10. Convergence behavior and metric evaluation of the coherent solution technique for 2 kHz trailing edge noise data.

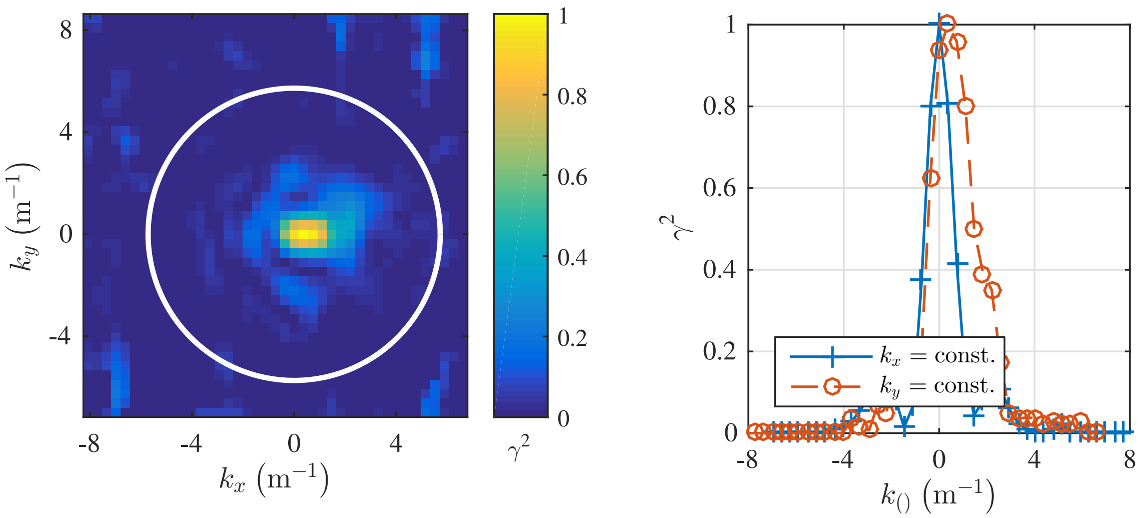

(a) coherence map

(b) k_x and k_y coherence slices

Figure 11. Analysis of computed coherence-squared relationships of the deconvolved wavenumber field, referenced to the trailing edge noise source center at $(k_x, k_y) = (0.37, 0)$ m^{-1}.

5. Summary and conclusions

A deconvolution technique for a class of shift-invariant problems is derived and presented. The technique operates on two-dimensional microphone phased array data in the wavenumber-frequency domain and is designed to handle acoustic fields of arbitrary coherence structure. The deconvolution method is based on an iterative solver which utilizes a four-dimensional FFT to perform fast convolutions, providing improved scaling with problem size when compared to matrix methods. An updated constraint model is proposed and implemented, and an iterative relaxation parameter defined.

The updated constraint model follows attempts at applying constraints in coherent deconvolution analysis, but handles the diagonal terms of the covariance array differently. The model appears to provide improved performance when compared to a simple covariance inequality constraint. The updated constraint model also provides improved consistency and stability to convergence metrics. The improved stability allows for quantifiable convergence analysis. The relaxation parameter calculation successfully generates parameters which provide accelerated convergence when compared to previous work, while maintaining algorithm stability for positive semidefinite coefficient matrices. It is found that application of diagonal removal may lead to circumstances where the iterative solver is unstable regardless of relaxation parameter. Under these circumstances, the analysis grid must be re-defined.

The coherent deconvolution technique is applied to two data sets, using tools and conclusions drawn from a detailed analysis of various simulated data sets. The first of these simulates a closed test section wind tunnel measurement, while the second uses experimental data from an open-jet wind tunnel. When the closed test section data suffer from strong simulated boundary layer contamination, the coherent deconvolution technique fails to adequately capture sensible values for metrics of interest. This is in disagreement with behavior seen with more simple simulated configurations. With the experimental data, the technique recovers the expected acoustic level at the array center. It also shows some ability to determine qualitative coherence characteristics of trailing edge noise. Specifically, the method shows a larger streamwise coherence scale than the spanwise scale, in agreement with existing published results.

Overall, the proposed deconvolution technique is successful in analyzing many types of acoustic fields. The updated constraints, while not proven to be the best, provide sufficient information for tracking convergence. A new convergence criterion, where the change in solution must have a two order-of-magnitude reduction after entering a power law relationship with the solution residual (and the residual is decreasing), appears to hold for all of the analyzed acoustic fields. This criterion clearly sets where metrics of interest stop changing, whether or not they are strictly correct. When the criterion is not met, metrics clearly show the process is experiencing difficulties. The integration boundary calculations successfully extract source powers when data are not overly-contaminated. The presented work demonstrates the ability to analyze microphone phased array data in the wavenumber-frequency domain and extract both qualitative and quantitative information about the acoustic field, although significant limitations are exposed in this study.

One of the stronger conclusions regarding limitations is that coherent deconvolution in its current form may require significant investment in grid layout studies to successfully extract useful acoustic data. Some grid layouts can be excluded based on the array geometry and general processing parameters, once it is determined that $\mathbf{A}$ is not positive semidefinite. Others may only be found to be problematic once the algorithm is in use, and energetic sidelobe structures appear on the deconvolution boundary as with the trailing edge noise experiment data. Even with an acceptable grid, masking of acoustic sources of interest with strong contamination, such as that shown with the simulated data of a point source and its image in flow, may not show a successful recovery of acoustic parameters of interest. Even with a successful recovery of integrated acoustic parameters, aspects of the array design appear to occasionally manifest in the deconvolution results even though deconvolution is intended to remove the array design from the data. Finally, for acoustic fields generated by non-discrete sets of plane waves, while the center of the microphone phased array appears to be a reasonable reference point for evaluating magnitude and phase relationships, this effort does not determine whether such a reference is truly correct.

That said, coherent deconvolution is required to assess coherence and phase relationships between sources. The analysis technique evaluated here provides a tool which allows for coherent deconvolution with reduced computation and storage requirements when compared to other methods. For several simulated data sets the algorithm is shown to accurately recover coherence and phase relationships.

Several recommendations stem from this work for anyone wishing to attempt to use wavenumber-frequency coherent deconvolution. First, while tracking the change in solution and residual does not allow a user to determine the correctness of a solution, it does allow a user to determine the convergence of a solution. Therefore it is always worthwhile to extract these quantities during processing. Second, if at all possible it appears that wavenumber-frequency data processing should be considered in the design of a microphone phased array to be used for such. A brief evaluation of the wavenumber-frequency transform of the acoustic field of a nearby centered point source may reveal undesirable structures in the array sampling pattern which can be modified in the design process. These may come with a trade-off for more conventional array signal processing requirements, so a cost-benefit decision could be required. Finally, considering the physics of the acoustic propagation in defining integration boundaries is extremely valuable. When deconvolution is successful these physics-based boundaries allow accurate capture of magnitude and phase relationships between a point source and its image, even when both manifest as distributed wavenumber fields due to their proximity to the microphone phased array.

References

[1] T. F. Brooks, W. M. Humphreys, A deconvolution approach for the mapping of acoustic sources (DAMAS) determined from phased microphone arrays, Journal of Sound and Vibration 294 (2006) 856–879.

[2] R. P. Dougherty, Extensions of DAMAS and benefits and limitations of deconvolution in beamforming, AIAA-2005-2961, 11th AIAA/CEAS Aeroacoustics Conference, Monterey, CA, 2005.

[3] T. Yardibi, J. Li, P. Stoica, L. Cattafesta, Sparsity constrained deconvolution approaches for acoustic source mapping, Journal of the Acoustical Society of America 123 (2008) 2631–2642.

[4] P. Sijtsma, CLEAN based on spatial source coherence, International Journal of Aeroacoustics 6 (2007) 357–374.

[5] T. Yardibi, J. Li, P. Stoica, N. S. Zawodny, L. Cattafesta, A covariance-fitting approach for correlated acoustic source mapping, Journal of the Acoustical Society of America 127 (2010) 2920–2931.

[6] P. A. Ravetta, R. A. Burdisso, W. F. Ng, Noise source localization and optimization of phased-array results, AIAA Journal 47 (2009) 2520–2533.

[7] T. F. Brooks, W. M. Humphreys, Extension of DAMAS phased array processing for spatial coherence determination (DAMAS-C), AIAA-2006-2654, 12th AIAA/CEAS Aeroacoustics Conference, Cambridge, MA, 2006.

[8] T. Suzuki, l_1 generalized inverse beam-forming algorithm resolving coherent/incoherent, distributed and multipole sources, Journal of Sound and Vibration 330 (2011) 5835–5851.

[9] R. P. Dougherty, Improved generalized inverse beamforming for jet noise, AIAA-2011-2769, 17th AIAA/CEAS Aeroacoustics Conference, Portland, OR, 2011.

[10] J. S. Bendat, A. G. Piersol, "Stationary Random Processes" in Random Data Analysis and Measurement Procedures, John Wiley & Sons, Inc., New York, NY, 3rd edition, 2000.

[11] V. Fleury, J. Bulté, R. Davy, Determination of acoustic directivity from microphone array measurements using correlated monopoles, AIAA-2008-2855, 14th AIAA/CEAS Aeroacoustics Conference, Vancouver, CA, 2008.

[12] L. M. Brekhovskikh, "Reflection and Refraction of Spherical Waves" in Waves in Layered Media, Academic Press, Inc., 1960.

[13] E. G. Williams, "Plane Waves" in Fourier Acoustics: Sound Radiation and Nearfield Acoustical Holography, Academic Press, Inc., 1999.

[14] D. H. Johnson, D. E. Dudgeon, "Apertures and Arrays" in Array Signal Processing: Concepts and Techniques, Prentice Hall, Englewood Cliffs, NJ, 1993.

[15] E. G. Williams, "Fourier Transforms & Special Functions" in Fourier Acoustics: Sound Radiation and Nearfield Acoustical Holography, Academic Press, Inc., 1999.

[16] J. Capon, High-resolution frequency-wavenumber spectrum analysis, Proceedings of the IEEE 57 (1969) 1408–1418.

[17] R. P. Dougherty, "Beamforming in Acoustic Testing," chapter 2 in Aeroacoustic Measurements, T. J. Mueller, Ed., Springer-Verlag, Berlin, Heidelberg & New York, 2002.

[18] C. Bahr, L. Cattafesta, Wavespace-based coherent deconvolution, AIAA-2012-2227, 18th AIAA/CEAS Aeroacoustics Conference, Colorado Springs, CO, 2012.

[19] N. J. Higham, Computing a nearest symmetric positive semidefinite matrix, Linear Algebra and its Applications 103 (1988) 103–118.

[20] J. D'Errico, nearestSPD (http://www.mathworks.com/matlabcentral/fileexchange/42885-nearestspd, last accessed December 11, 2014), 2013.

[21] M. Frigo, S. G. Johnson, Pruned FFTs (http://www.fftw.org/pruned.html, last accessed December 11, 2014), 2007.

[22] K. E. Atkinson, An Introduction to Numerical Analysis, John Wiley & Sons, Inc., 2nd edition, 1989.

[23] D. C. Sorensen, Implicitly Restarted Arnoldi/Lanczos Methods for Large Scale Eigenvalue Calculations, Technical Report NASA CR-198342, Institute for Computer Applications in Science and Engineering, 1996.

[24] T. F. Brooks, W. M. Humphreys, G. E. Plassman, DAMAS processing for a phased array study in the NASA Langley Jet Noise Laboratory, AIAA-2010-3780, 16th AIAA/CEAS Aeroacoustics Conference, Stockholm, Sweden, 2010.
[25] M. Frigo, S. G. Johnson, The design and implementation of FFTW3, Proceedings of the IEEE 93 (2005) 216–231.
[26] C. J. Bahr, N. S. Zawodny, B. Bertolucci, J. Li, M. Sheplak, L. N. Cattafesta, A plasma-based non-intrusive point source for acoustic beamforming applications, Journal of Sound and Vibration 344 (2015) 59–80.
[27] B. Arguillat, D. Ricot, C. Bailly, G. Robert, Measured wavenumber: Frequency spectrum associated with acoustic and aerodynamic wall pressure fluctuations, Journal of the Acoustical Society of America 128 (2010) 1647–1655.
[28] D. Papamoschou, S. Mayoral, Modeling of jet noise sources and their diffraction with uniform flow, AIAA-2013-0326, 51st AIAA Aerospace Sciences Meeting, Dallas/Ft. Worth, TX, 2013.
[29] G. M. Corcos, Resolution of pressure in turbulence, Journal of the Acoustical Society of America 35 (1963) 192–199.
[30] C. Bahr, J. Li, L. Cattafesta, Aeroacoustic measurements in open-jet wind tunnels - an evaluation of methods applied to trailing edge noise, AIAA-2011-2771, 17th AIAA/CEAS Aeroacoustics Conference, Portland, OR, 2011.
[31] R. K. Amiet, Refraction of sound by a shear layer, Journal of Sound and Vibration 58 (1978) 467–482.
[32] T. F. Brooks, T. H. Hodgson, Trailing edge noise prediction from measured surface pressures, Journal of Sound and Vibration 78 (1981) 69–117.
[33] J. R. Underbrink, Practical Considerations in Focused Array Design for Passive Broad-Band Source Mapping Applications, Master's thesis, The Pennsylvania State University, State College, PA, 1995.
[34] D. T. Blackstock, "Detailed Development of the Acoustical Wave Equation" in Fundamentals of Physical Acoustics, John Wiley & Sons, Inc., New York, NY, 2000.
[35] D. H. Johnson, D. E. Dudgeon, "Signals in Space and Time" in Array Signal Processing: Concepts and Techniques, Prentice Hall, Englewood Cliffs, NJ, 1993.

Appendix A Simulated data study

A detailed study of the technique with various simulated data is presented. The intent of this study is to show the behavior of this deconvolution method for increasingly-complex acoustic fields, as well as provide examples as to how results might be analyzed and reduced for discussion.

A.1 Plane wave analysis

Sample results for simulated plane wave fields, which are identically shift-invariant, are presented first. All simulation results are generated by constructing a simulated CSM, transforming the data to the wavenumber domain, and then applying the deconvolution method. Comparison is made between the generalized coherence formulation and one which assumes incoherent-only sources and simply enforces a positivity constraint on computed variances. Grid scales are initially selected for rapid assessment of algorithm performance, rather than detailed analysis of a realistic acoustic field. The effect of diagonal removal on processing is addressed, but diagonal removal is incorporated in all plotted data. Fields of varying complexity are considered. All simulations use the microphone layout of the outer UFAFF array [26] mentioned in Section 3.5. Details of the array can be found in the reference, but in brief the array is a 0.74 m aperture, 5-arm log spiral design based on the methodology of Underbrink [33] consisting of 40 total microphones. As stated previously, the array has a 3-dB beamwidth in the wavenumber domain of $w = 1.47$ m^{-1}.

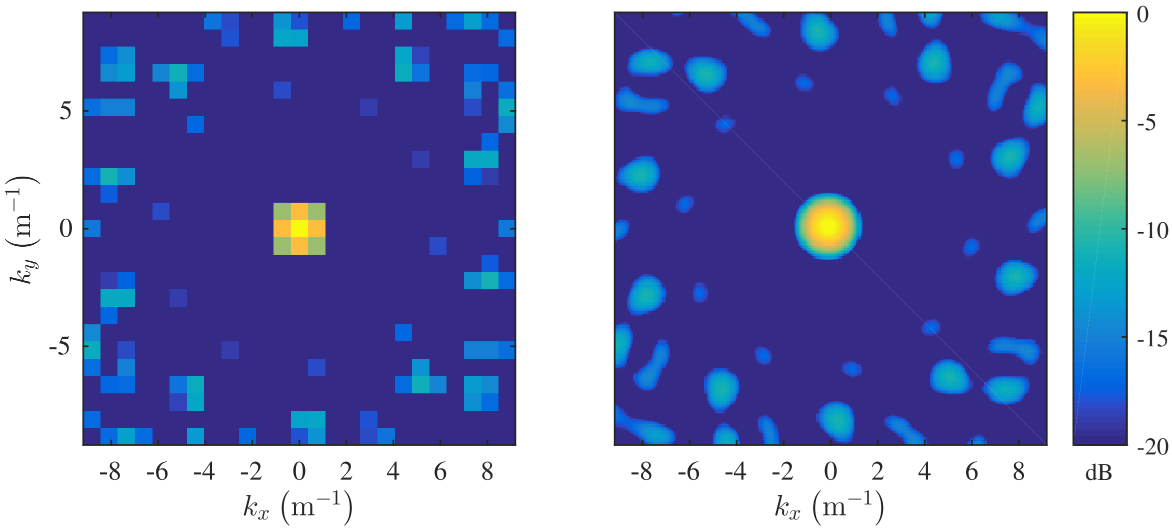

(a) $\Delta k_{()} = w/2$

(b) $\Delta k_{()} = w/20$

Figure A.1. Sampling function variances for large and small grid spacings.

The sampling function from Eq. 12 is shown for $k_x = k_\xi$ and $k_y = k_\eta$ in Fig. A.1, with a grid spacing of $\Delta k_{()} = w/2$ in Fig. A.1a and $\Delta k_{()} = w/20$ in Fig. A.1b. Data are shown on a 20 dB color scale and normalized to unity gain. Decibel scales of subsequent pressure plots are normalized by 20 μPa. Note that as diagonal removal causes some of the computed variances from the wavenumber transform to become (non-physically) negative, these negative values are set to $-\infty$ dB in all figures for plotting purposes. As shown, a low resolution calculation captures the major features of the array measurement but misses fine details. Levels of small sidelobes such as the innermost ring appear underpredicted by the low resolution map.

A.2 Isolated plane wave

The first case considered is a single, normal-incidence plane wave, corresponding to a point in wavenumber space with $(k_x, k_y) = (0, 0)$ m^{-1}. This case is chosen to assess algorithm characteristics with respect to some of the choices made in the deconvolution process. The plane wave is simulated with an amplitude of 100 dB. The simulation parameters use the more coarse sampling grid from Fig. A.1a. The grid domain is set to $n_{k,()} = 7$ points and $n_{s,()} = 13$ points, which for the spacing of $\Delta k_{()} = w/2$ yields $k_{min,()} =$ -2.21 m^{-1} and $k_{max,()} = 2.21$ m^{-1}. Due to the simple nature of this case, the wavenumber-frequency data for $\tilde{P}$ and $\tilde{Q}$ are not plotted. The variances of $\tilde{P}$ appear identical to the sampling function in Fig. A.1a, albeit with a different peak value and a smaller grid. The deconvolved variances of $\tilde{Q}$ appear as a single point at $(k_x, k_y) = (0, 0)$ m^{-1} with a magnitude of 100 dB, regardless of the combination of method options.

Table A.1 shows the relaxation parameter and convergence behavior for different combinations of configurations for the solution technique for coherent and incoherent solvers. Convergence in this case is defined as $v < 10^{-15}$, as the lowest order of magnitude all four combinations of parameters achieve. As would be expected, using a coherent method for an incoherent problem is an unnecessary increase in computational expense. For a given wavenumber domain, the relaxation parameter dramatically increases along with the number of iterations required for convergence.

Notably, diagonal removal has a strong effect on the convergence behavior of the coherent method. There is a significant reduction in the required iteration count for convergence when applying diagonal removal. This reduction is accompanied by an increase in the relative error for the same convergence criterion. As mentioned previously, the convergence rate of the Richardson iteration method is dependent on the condition number of $\mathbf{A}$. This is shown in Table A.1, along with the resultant relaxation parameter. For this grid, diagonal removal leads to a reduction in condition number and thus reduction in relaxation parameter, accelerating convergence. This comparison is not an attempt to show a universal benefit to diagonal removal as long as a positive semidefinite $\mathbf{A}$ can be computed. It is simply an example evaluation of the influence of the parameter on solver behavior. As much aeroacoustic array analysis occurs using diagonal removal to mitigate the influence of microphone self-noise, the remainder of the case analyses will apply the technique.

Table A.1. Relaxation parameters, condition numbers, iterations to converge (rounded), and relative error for varying method options for a normal-incidence plane wave with $n_{k,()} = 7$ and $\Delta k_{()} = w/2$ grid spacing.

	Coherent Method	Incoherent Method
No Diagonal Removal	$a = 35.1$; $\mathrm{cond}(\mathbf{A}) = 4.93 \times 10^3$ 23,500 iterations; $u^{(i)} = 4.02 \times 10^{-14}$	$a = 2.00$; $\mathrm{cond}(\mathbf{A}) = 16.0$ 262 iterations; $u^{(i)} = 2.60 \times 10^{-15}$
Diagonal Removal	$a = 32.4$; $\mathrm{cond}(\mathbf{A}) = 4.21 \times 10^3$ 10,800 iterations; $u^{(i)} = 1.16 \times 10^{-13}$	$a = 1.58$; $\mathrm{cond}(\mathbf{A}) = 10.0$ 204 iterations; $u^{(i)} = 2.85 \times 10^{-15}$

A.3 Partially-coherent discrete plane waves

A line of three plane waves of varying relative phase and coherence is simulated. The waves have a spacing of $w/2$ in the wavenumber domain. They lie along the k_x axis, with all $k_y = 0$. The covariance array of the simulated plane waves is given in terms of their k_x and k_ξ values in Table A.2. This covariance definition corresponds to each wave having a coherence-squared value of $\gamma^2 = 1/2$ with respect to its immediate neighbor, and the end waves having coherence-squared values of $\gamma^2 = 1/4$ with respect to each other. The waves have a $\pi/4$ phase lag with respect to their immediate neighbors, running left-to-right along the k_x axis. The central wave has a variance level of 100 dB, while the leftmost wave has a variance level of 94.0 dB and the rightmost wave has a variance level of 88.0 dB. This simulation encapsulates a wave field where one plane wave is dominant, all waves are partially-coherent with respect to each other, and adjacent waves are within a fraction of a beamwidth of each other. Plots of the variance from the initial wavenumber transform of the data, $\tilde{P}$ from Eq. (10), are shown in Fig. A.2 with grid spacings of $w/2$ (Fig. A.2a) and $w/20$ (Fig. A.2b).

Table A.2. Covariance relationships between plane waves simulated along the k_x axis.

$k_x \backslash k_\xi$ (m^{-1})	-1.47/2	0	1.47/2
-1.47/2	1	$\sqrt{2} \times e^{j\frac{\pi}{4}}$	$\frac{1}{4} \times e^{j\frac{\pi}{2}}$
0	$\sqrt{2} \times e^{-j\frac{\pi}{4}}$	4	$\frac{1}{\sqrt{2}} \times e^{j\frac{\pi}{4}}$
1.47/2	$\frac{1}{4} \times e^{-j\frac{\pi}{2}}$	$\frac{1}{\sqrt{2}} \times e^{-j\frac{\pi}{4}}$	$\frac{1}{4}$

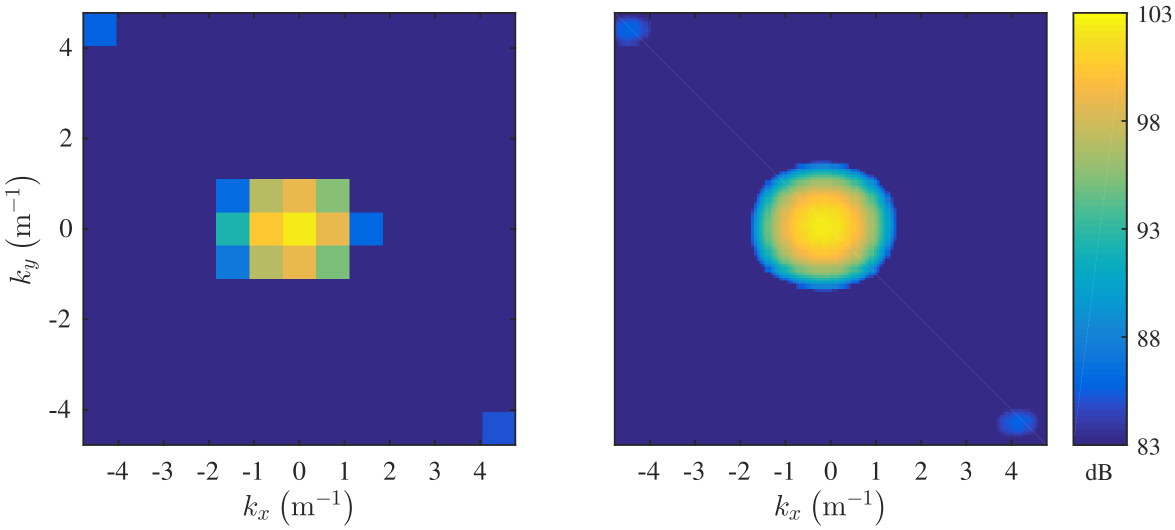

(a) $\Delta k_{()} = w/2$

(b) $\Delta k_{()} = w/20$

Figure A.2. Wavenumber transform variances computed for adjacent, partially-coherent plane waves for coarse and fine grid spacings.

A.3.1 Baseline grid

The initial grid is constructed with $\Delta k_{()} = w/2$, $n_{k,x} = 7$, and $n_{k,y} = 5$. This coarse grid completely captures the energetic region of Fig. A.2a and colocates grid points with true source wavenumbers. For linear convolution, $n_{s,x} = 13$ and $n_{s,y} = 9$ giving $a = 23.4$ for the coherent solver. The coarse grid size is selected for rapid assessment of algorithm characteristics for this type of problem.

Deconvolution results using both the proposed coherent method and incoherent equivalent are shown in

Fig. A.3, where convergence is again defined as $v < 10^{-15}$. Visually, the results appear similar. The coherent method in Fig. A.3a captures all three source variances correctly. However, the incoherent method in Fig. A.3b overestimates the center source at 101.6 dB, the left source at 96.1 dB, and slightly underestimates the right source at 87.9 dB.

An integrated level metric is defined as the sum of $\tilde{Q}$. For the incoherent method, this is simply the sum of the wavenumber variances of interest. For the coherent method, it is the sum of the entire covariance array within the wavenumber bounds of interest. This is equivalent to inverse-transforming the covariance wavenumber data back to the spatial domain at a coordinate of $(x, y, \xi, \eta) = (0, 0, 0, 0)$, and thus should be compared to the acoustic variance level at the array center. The true level at the array center is 103.1 dB. The integrated level of the coherent solution matches this to printed precision, and has a relative error (computed with the pressure-squared data) of 1.94×10^{-15}. The integrated level of the incoherent solution is 102.9 dB, with a relative error of -4.75×10^{-2}. On a decibel scale the difference is minor, but the integrated relative error difference is significant. Similarly, the solution relative error for the coherent method at convergence is $u = 2.46 \times 10^{-13}$, while for the incoherent method it is $u = 2.02 \times 10^{-2}$.

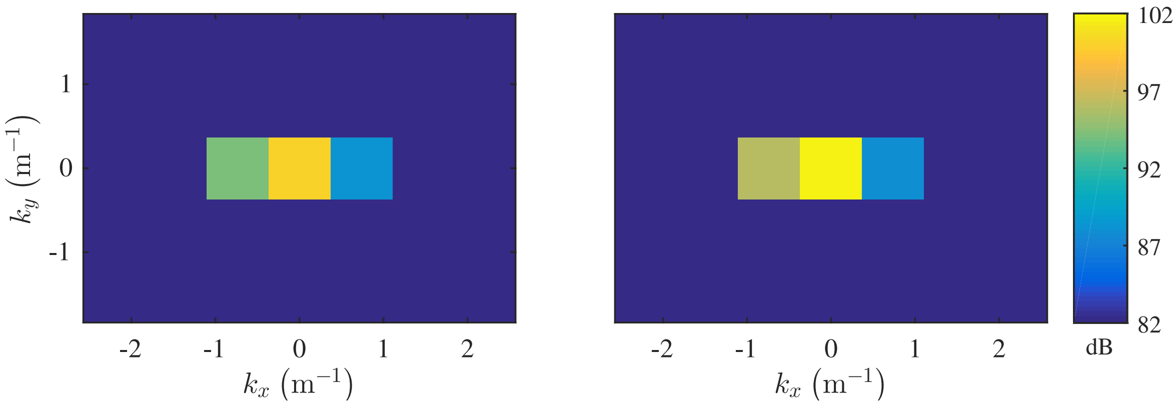

(a) coherent deconvolution - left-to-right levels of 94.0, 100, and 88.0 dB

(b) incoherent deconvolution - left-to-right levels of 96.1, 102, and 87.9 dB

Figure A.3. Variances from deconvolution of partially-coherent plane wave simulation using baseline $w/2$ spacing grid with both coherent and incoherent methods.

The improvement in error characteristics does carry significant extra cost, as seen with the broadside isolated wave case. Here, the incoherent method reaches convergence in 211 iterations. The coherent method takes just under 8.29×10^5 iterations. This definition of numeric convergence, based on these first two cases, is expected to scale such that reaching a stopping criterion of $v < 10^{-15}$ may be an impractical objective for many problems of interest. As such, the characteristics of several metrics calculated from the coherent deconvolution results are considered as functions of v to assess valid stopping criteria. These four metrics are:

1. u,
2. the integrated level relative error defined previously,
3. the ℓ^2 normalized error of the magnitudes of the wavenumber covariance matrix, and
4. the ℓ^2 normalized error of the phases of the wavenumber covariance matrix.

Since the wavenumbers of the input plane waves are known for this case, the normalized error calculations for the magnitude and phase only include grid points corresponding to the input plane waves, and only for the lower-triangular components of the covariance matrix as magnitudes are symmetric about the diagonal and phases exactly cancel.

The overall convergence behavior of the algorithm is shown in Fig. A.4a for both u and v. Both quantities experience an extremely steep roll-off initially, followed by a long period of logarithmic reduction. While there is an offset between the two, for the most part they trend together. Note that both quantities continue to reduce in magnitude after the pre-selected convergence criterion is first met. Metrics of interest as a function of v are shown in Fig. A.4b. For this case, u and the integrated level error trend together for much of the plot range, while the magnitude and phase errors trend together. Notably, all errors scale poorly with v for $v > 10^{-6}$, prior to the logarithmic roll-off regime of the plot. The integrated level error actually increases slightly for $10^{-5} > v > 10^{-6}$. This behavior, along with the high error levels of all tracked metrics, would suggest that $v = 10^{-6}$ is an insufficient convergence criterion for this case. The phase error appears to be the most strict error metric to consider, and it has a value of just above 1% for $v = 10^{-7}$ $\left(u = 2.5 \times 10^{-5}\right)$ and just above 0.1% for $v = 10^{-8}$ $\left(u = 2.5 \times 10^{-6}\right)$. Depending on the desired level of phase accuracy, this would suggest using either $v = 10^{-7}$ or $v = 10^{-8}$ as a convergence criterion for this case. These criteria are met at approximately 1.07×10^5 iterations and 1.97×10^5 iterations, respectively, requiring roughly 1/8 to 1/4 as many iterations as the initial convergence criterion of $v = 10^{-15}$.

A.3.2 Refined grid

The initial grid is refined to determine the deconvolution method's ability to separate discrete plane waves within a fraction of a beamwidth of each other. On the previous grid, the input plane waves occupied adjacent grid points. The refined grid is constructed with $\Delta k_x = w/4$, $n_{k,x} = 13$, so the true solution will have zero-variance grid points between the input plane waves. As the problem is defined and known to have sources only existing along the k_x axis, no k_y refinement is performed. The ability of the deconvolution method to handle different grid spacings in the k_x and k_y directions is utilized. For linear convolution, the updated grid size is $n_{s,x} = 25$, and the relaxation parameter becomes $a = 87.3$ for the coherent solver.

Deconvolution results using both the proposed coherent method and incoherent equivalent are shown in Fig. A.5, where convergence is still defined as $v < 10^{-15}$. Unlike the baseline grid, the results for the coherent

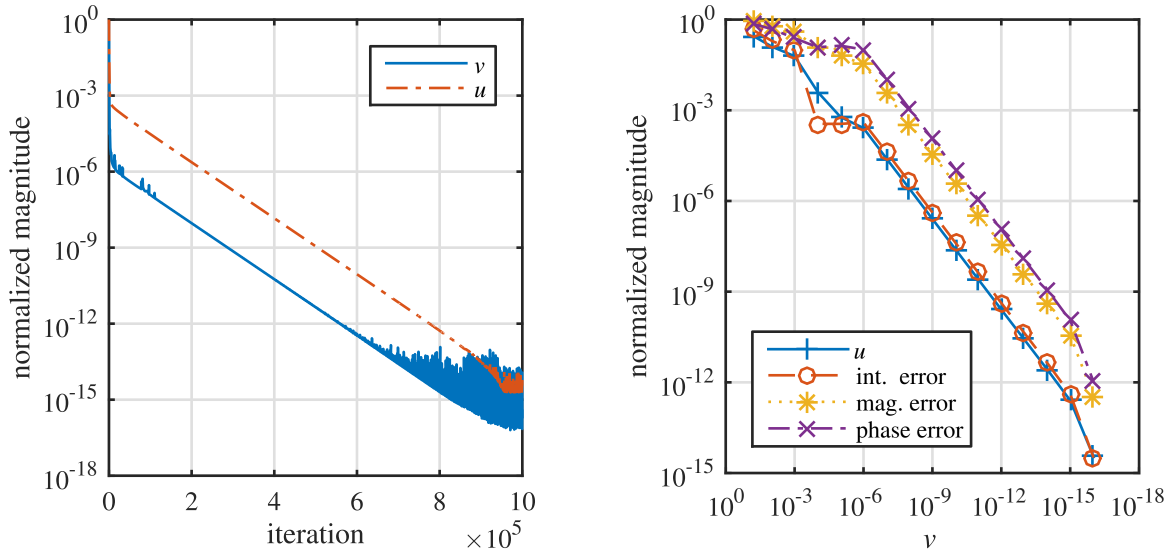

(a) solution procedure norms

(b) metrics as a function of v

Figure A.4. Convergence behavior and metrics comparison of the coherent solution technique for the baseline grid of the partially-coherent plane wave simulation.

method in Fig. A.5a differ significantly from those for the incoherent method in Fig. A.5b. The coherent method captures the correct source levels and locations. The incoherent method slightly underpredicts the level of the plane wave at $(k_x, k_y) = (0, 0)$ as 99.2 dB rather than 100 dB. The incoherent method also locates false plane waves at $k_x = \pm w/4$ and off the k_x axis at $(k_x, k_y) = (3w/4, w/2)$, and underpredicts the left plane wave at 91.4 dB while completely missing the plane wave on the right.

The integrated level metric is computed. As the source characteristics are unchanged, the level at the array center is still 103.1 dB. As with the previous grid, the integrated level of the coherent solution matches the array center level to printed precision, with a relative error of -2.37×10^{-15}. The integrated level of the incoherent solution is 102.9 dB, as it was for the baseline grid. The relative error is slightly higher with a value of -5.56×10^{-2}. The solution relative error for the coherent method at convergence is $u = 3.98 \times 10^{-12}$, while that for the incoherent method at convergence is $u = 8.19 \times 10^{-3}$.

Solutions on this grid are significantly more expensive to compute than on the previous grid. The incoherent method reaches convergence in 1.64×10^4 iterations. The coherent method takes just over 1.69×10^8 iterations. Overall convergence behavior is plotted in Fig. A.6a. It appears that while the method can successfully separate discrete plane waves within a fraction of w of each other, it requires significant effort to do so. Code run times can vary greatly depending on hardware- and software-specific details, but as a qualitative example this research implementation could perform approximately 50 million iterations per day for a grid of this size, yielding a total run time of just under 3 1/2 days to reach $v = 10^{-15}$. Clearly

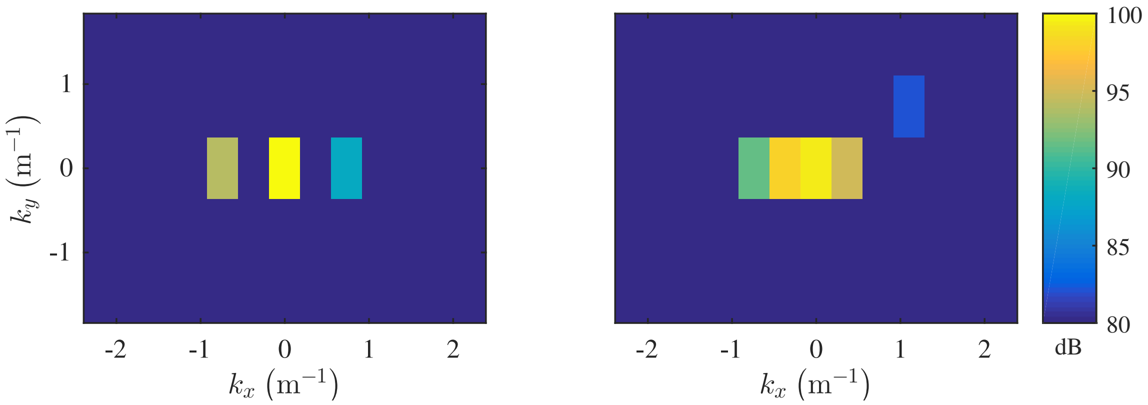

(a) coherent deconvolution - left-to-right levels of 94.0, 100, and 88.0 dB

(b) incoherent deconvolution- left-to-right levels (at actual source locations) of 91.4, 99.2, and $-\infty$ dB

Figure A.5. Variances from deconvolution of partially-coherent plane wave simulation using refined ($\Delta k_x = w/4$) spacing grid with both coherent and incoherent methods.

this is excessive for a narrowband analysis technique, so the additional metrics from the baseline grid are revisited to assess error characteristics for more relaxed stopping criteria.

Metrics are plotted in Fig. A.6b. Details of the behavior differ from the baseline grid solution. However, overall trending is similar. All errors scale poorly for $v > 10^{-6}$. Error in the integrated power does not roll off in a uniform fashion below this, but does decrease. Other metrics have a roughly-uniform roll-off below $v < 10^{-7}$. For this case, error in the source magnitude is slightly higher than phase. Both of these errors are above 10% for $v = 10^{-7}$. For $v = 10^{-9}$ ($u = 4.25 \times 10^{-6}$), the magnitude error is 1.59% and the phase error is 0.62%. By $v = 10^{-10}$ ($u = 4.60 \times 10^{-7}$), the magnitude error is 0.14% and the phase error is 0.03%, meeting the more stringent criteria considered for the baseline grid.

Unfortunately, the algorithm requires a reduction in v of two orders-of-magnitude more than that required for the baseline grid for the desired error characteristics, so a uniform criterion is not determined by the values of u or v. However, it appears that for both the baseline grid and refined grid, 1% error in the magnitude and phase is achieved when an order of magnitude reduction in v has occurred in the regime where v has a power law relationship with u (illustrated with log-log plots for subsequent test cases). Similarly, 0.1% error is achieved for a two order-of-magnitude reduction in this regime. For this case 1% error is reached near 55 million iterations, while 0.1% error is reached near 80 million iterations. For these two cut-offs, iteration requirements thus lie between just under 1/3 to just under 1/2 of the number needed for the initial numeric convergence selection of $v = 10^{-15}$.

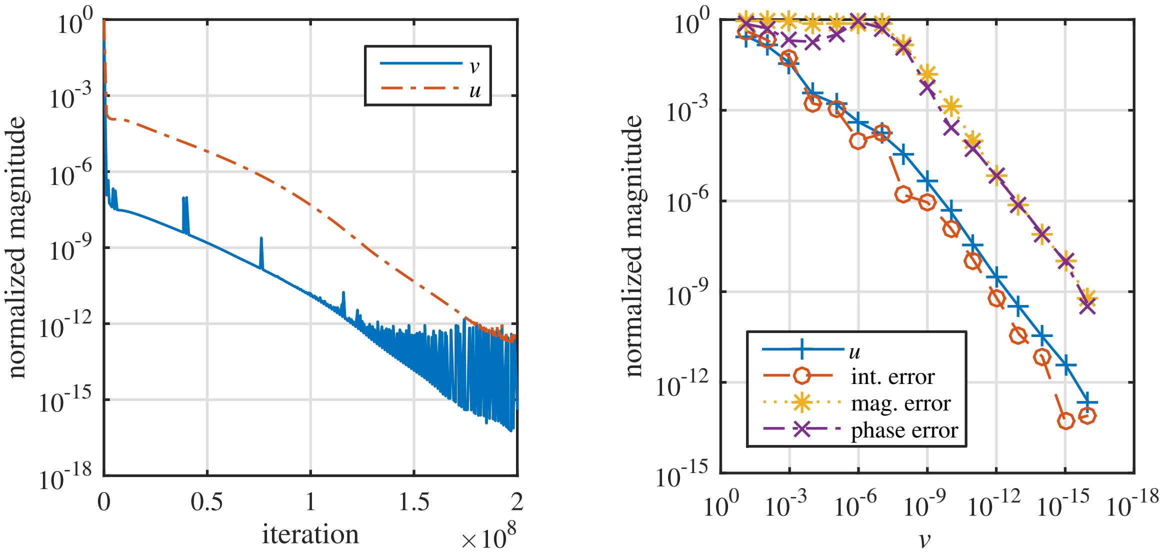

(a) solution procedure norms

(b) metrics as a function of v

Figure A.6. Convergence behavior and metrics comparison of the coherent solution technique for the refined grid of the partially-coherent plane wave simulation.

A.3.3 Refined grid - offset plane waves

The previous two grids located the plane waves at wavenumbers which exactly match points within the scan grid. The plane wave wavenumbers are now offset by $w/8$ in the k_x direction to lie halfway between wavenumbers in the refined grid. This is an important test case as, in general use, it is unlikely that a wave direction of arrival will precisely colocate with a wavenumber-domain grid point. The new source wavenumbers are $k_x = -3w/8$, 0, and $5w/8$, with all k_y remaining zero. All other characteristics of the sources remain unchanged, and the grid layout is identical to the refined grid of the previous subsection.

Deconvolution results are shown in Fig. A.7. The coherent simulation fails to converge. v drops below 10^{-9} after 3.86×10^7 iterations. It still remains above 10^{-10} after 1.25×10^9 iterations, or 25 days of wall time. As shown in Fig. A.8a, u remains above 10^{-5} and never enters a power law relationship with v. The coherent results show plane waves on either side of the true wavenumbers of each wave, as might be expected. The incoherent results focus the majority of the plane wave field at the center source area, and show waves at spurious wavenumbers off the $k_y = 0$ axis. The incoherent method drops below $v = 10^{-15}$ after 1.90×10^4 iterations, with u leveling off at 7.78×10^{-3}.

Metrics are computed as they were for the refined grid simulation. However, errors are computed based on the assumption that summing the grid points adjacent to a given plane wave wavenumber should yield the correct acoustic levels. Covariances are computed similarly. This is a first step at defining integration region bounds, which are discussed in more detail later. Metrics are plotted in Fig. A.8b. As demonstrated with

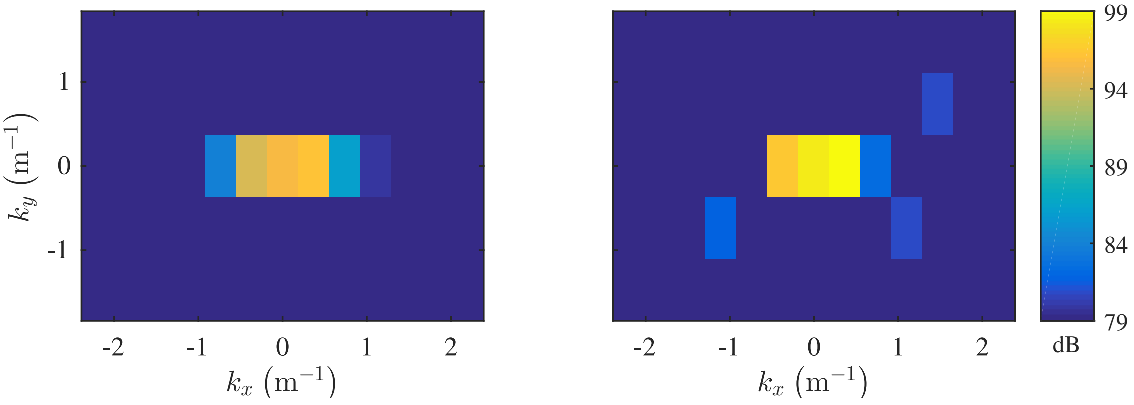

(a) coherent deconvolution

(b) incoherent deconvolution

Figure A.7. Variances from deconvolution of partially-coherent plane wave simulation with true wavenumbers between grid points using both coherent and incoherent methods.

the initial grid refinement, if u and v are not related by a power law then the error behavior is poor. Overall integrated power error is reasonable, but the individual plane wave component estimates significantly differ from true values to a degree in which they could be considered totally unreliable. Additionally, they appear to experience significant change even when v becomes small. While behavior may improve for smaller v, from a practical standpoint it makes little sense to extend the case evaluation beyond one and a quarter billion iterations. Resolving the component details of a problem consisting of mixed-coherence plane waves arriving from directions halfway between grid points appears beyond the capability of this algorithm, at least for this array and grid definition. This does suggest, however, that such observed behavior of u and v would indicate the need to alter the wavenumber grid of interest in some way.

A.4 General application

Simulated plane wave results demonstrate the algorithm's ability to extract quantitative information regarding the statistical relationship between sources, provide some indication of convergence criteria, and demonstrate how to assess when a given problem definition will not converge. More general application to non-planar wave fronts is now considered. This is done for both an isolated point source and a point source with an ideal reflection.

A.5 Isolated point source

The isolated point source is centered over the array and located 1.5 m away from the array center at a source coordinate of (0,0,1.5) m. This location is approximately twice the array aperture and allows for a moderately-curved wavefront to be observed by the array. The source is scaled such that its acoustic field has a level of 100 dB at the array center. Frequency selection involves some trade offs. In traditional

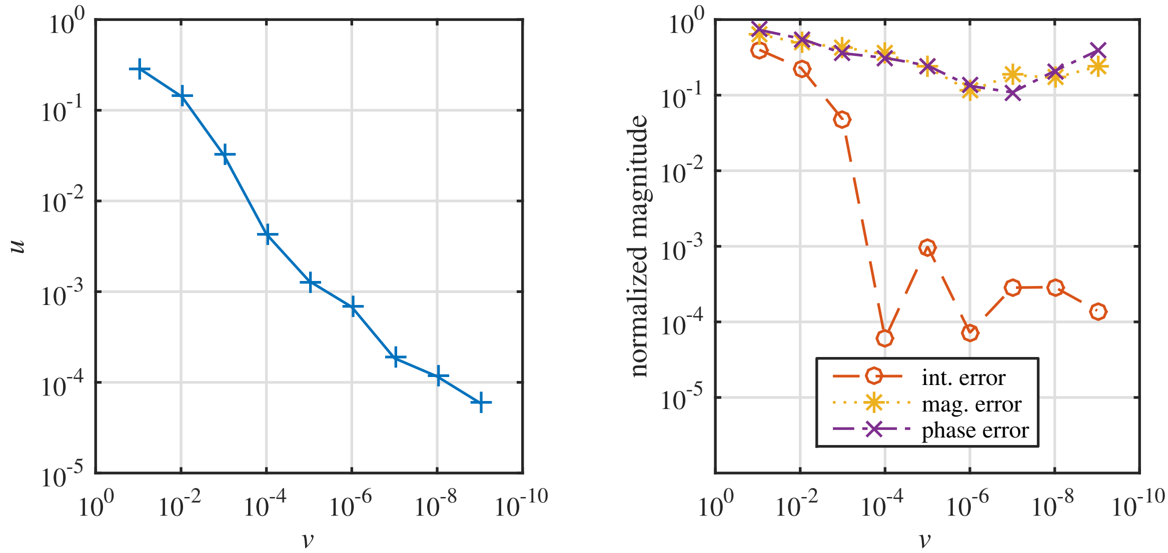

(a) u as a function of v

(b) metrics as a function of v

Figure A.8. Convergence behavior and metrics comparison of the coherent solution technique for the offset plane wave simulation.

aeroacoustic deconvolution analysis, methods often suffer poor behavior at low frequencies, depending on array size and source location. At higher frequencies, as mentioned earlier, it becomes computationally-cumbersome to analyze the entire acoustic radiation domain with the coherent method. For this particular case, a frequency of $f = 2$ kHz is selected, and the speed of sound is set to $c_0 = 343$ m/s.

The acoustic field of this point source will appear as a distribution of plane waves. The wavenumber-frequency domain grid is constructed to capture the entire acoustic radiation circle and extend at least $w/2$ beyond $k_0 = 5.83$ m^{-1}. $\Delta k_{()}$ is set to 25% of the main lobe beamwidth or $w/4$. The resultant grid has $n_{k,()} = 37$ points, with $k_{min,()} = -6.62$ m^{-1} and $k_{max,()} = 6.62$ m^{-1}, and is shown in Fig. A.9b. While the minimum $n_{s,()}$ for linear convolution is 73, $n_{s,()} = 75$ for this simulation as many FFT libraries show improved performance for transform lengths having small prime factors. The resultant relaxation parameter is $a = 2.49 \times 10^3$ for the coherent solver.

A comment is required regarding behavior of the point source data and frequency selection. The wavenumber transform variances of the point source data, $\tilde{P}$ from Eq. (10), are shown for several frequencies in Fig. A.9. The two higher-frequency grids show a pentagonal shape for what should be a perfectly axisymmetric wavenumber distribution. As mentioned previously, the UFAFF aeroacoustic array is a 5-arm log spiral design. As would be expected, the array layout plays a strong role in the wavenumber transform. However, the layout also plays a strong role in the deconvolution results. As seen subsequently, the deconvolved 2 kHz data show some aspects of a pentagonal shape. Not shown are attempts at a coherent deconvolution of the 1 kHz grid. The algorithm struggled and showed no well-defined convergence progress (oscillatory v, and $u > 0.1$). It appeared to be driving towards a single strong plane wave at $(k_x, k_y) = (0, 0)$ with noticeable five-fold axisymmetric artifacts. Various other grid sizes and densities showed similar behavior for 1 kHz input data. This could suggest that, as with conventional deconvolution, low-frequency analysis may be problematic. It could also suggest that the conventional design rules for aeroacoustic arrays may yield geometries which are sub-optimal for wavenumber-frequency deconvolution when applied to sources near the array. The 2 kHz data showed more agreeable convergence behavior, and are thus selected for further analysis to highlight how well-behaved data can be handled. The 4 kHz data are not analyzed in detail due to the computational expense of running the shown $n_{k,()} = 69$ point grid.

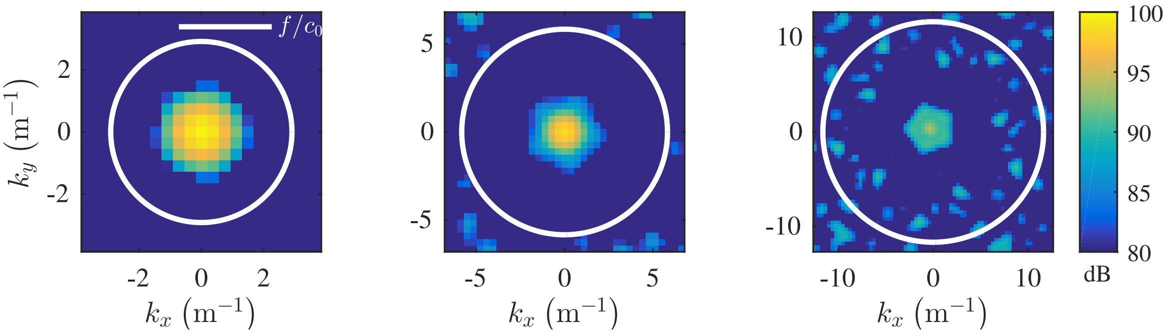

(a) 1 kHz (b) 2 kHz (c) 4 kHz

Figure A.9. Wavenumber transform variance as a function of frequency for a point source located near the UFAFF array, with grid spacing $\Delta k_{()} = w/4$.

For this and subsequent cases, no obvious exact solution is available for error calculation. The complete wavenumber-frequency spectrum of a point source projected on a plane is inappropriate, as that spectrum requires an infinite measurement plane. Numeric transformation of the point source wave field projected on a finite disk may or may not be a viable metric for comparison, but is cumbersome and has no guarantee of providing a correct reference field. In this work simplified power metrics, such as the level at the array center microphone or the average level across the array of microphones, are considered. While these do not provide an assessment of true error behavior for the deconvolution process, they do provide references for overall trending and convergence of algorithm performance, as well as a sanity check on the deconvolution results.

For a single source, integrated levels can be considered by summing the overall deconvolution domain. However a wavenumber filtering technique is implemented to separate multiple acoustic sources, as well as separate acoustic and hydrodynamic wavenumber domains. This is done by defining a filter as a function of grid point, $\Psi(k_x, k_y)$. The total filtered integrated power for a given source region is then defined as

$$\tilde{Q}_{source} = \sum \Psi_{source}(k_x, k_y)\, \Psi_{source}(k_\xi, k_\eta)\, \tilde{Q}(k_x, k_y, k_\xi, k_\eta)\,, \tag{A.1}$$

where summation occurs over all grid points. Details on the construction of Ψ are given in Appendix B.

Deconvolution results using both the proposed coherent method and incoherent equivalent are shown in Fig. A.10. For this case, v drops below 10^{-12} before both v and u stop changing with increased iteration count. This occurs in just under 1.70×10^4 iterations. As shown in Fig. A.11a, $v = 10^{-12}$ corresponds to $u = 6.86 \times 10^{-12}$ for the coherent method. The incoherent method (convergence characteristics reported but not plotted) also reaches $v = 10^{-12}$ after just over 2.19×10^4 iterations, although it continues to decrease to below 10^{-16}. The value of u reaches a minimum of 9.23×10^{-2} for the incoherent method. The coherent results in Fig. A.10a show a plane wave distribution mostly residing within the geometric angle integration boundary described in Appendix B. The incoherent results show a plane wave arriving from the array-normal direction.

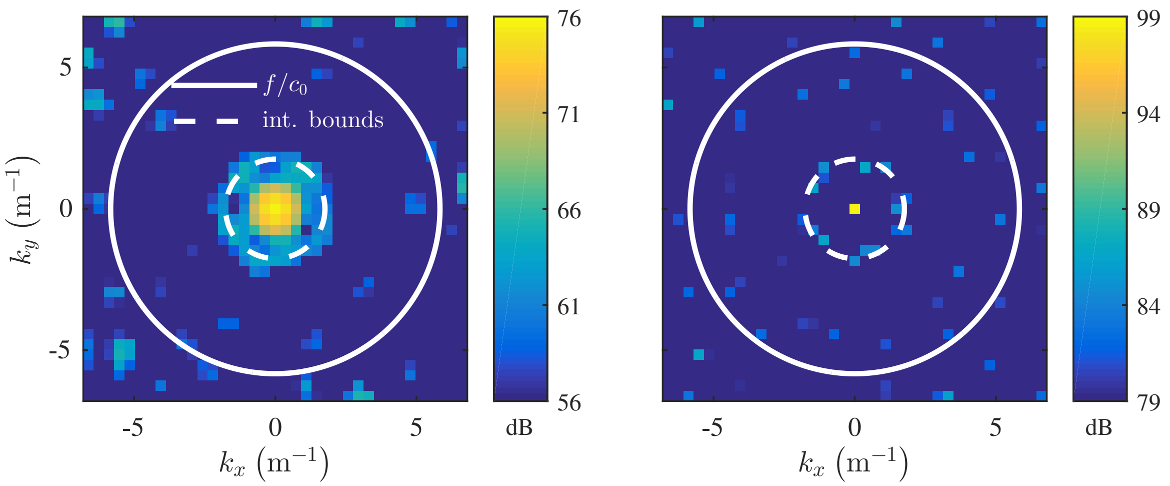

(a) coherent deconvolution (b) incoherent deconvolution

Figure A.10. Variances from deconvolution of point source data using $\Delta k_{()} = w/4$ spacing grid with both coherent and incoherent methods.

Three different metrics are plotted in Fig. A.11b. The first sums the entire solution domain. The second defines Ψ to isolate the acoustic radiation domain from the rest of the solution. The third defines Ψ to isolate the source location based on the geometric angles described in Appendix B and plotted as the dashed bounds in Fig. A.10. Metrics are now calculated in dB rather than as relative errors. The dB values are compared to the array center level and the array average level (calculated as the mean of the Pa^2 powers of each individual microphone). It can be readily argued that calculating the overall sum level for the deconvolution process, including the region outside the acoustic radiation circle, makes little sense. As the array is over 8 wavelengths away from the point source, evanescent components of the wavenumber spectrum should be completely suppressed. However, a case could be made for either of the other metrics being reasonable attempts at computing the power seen by the array. All three metrics show significant variation for $v > 10^{-5}$. All have reached a converged value by $v = 10^{-6}$, which corresponds to a two order-of-magnitude reduction in v in the regime where v has a power law relationship with u, shown in Fig. A.11a. None of the metrics precisely match the array center level of 100 dB or the array average level of 99.9 dB, indicating that these simple levels are not ideal choices for direct comparison with wavenumber-frequency domain data in this situation. The acoustic radiation sum and source angle integration boundary sum agree to within .026 dB for $v < 10^{-6}$, which appears reasonable for a case with a single isolated acoustic source.

Integrated metrics for the incoherent solution are also computed at convergence. Here, summing the entire solution yields 103.6 dB. Summing the acoustic radiation domain yields 102.3 dB. Summing the geometric angle region yields 100.1 dB. In logarithmic terms these values are close to the array center level and array average level, and the source angle integration boundary sum comes the closest of any method, coherent or incoherent, to matching the array center and array average level.

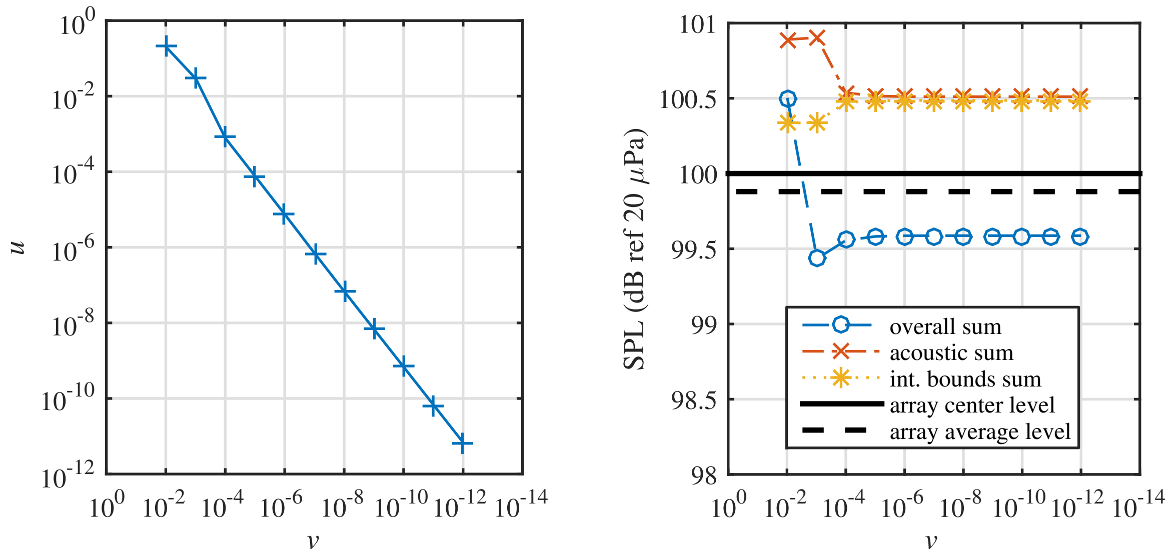

(a) u as a function of v

(b) metrics as a function of v

Figure A.11. Convergence behavior and metrics comparison of the coherent solution technique for the point source simulation.

A.6 Point source with a reflection

The acoustic field for the isolated point source is now modified by the inclusion of an ideal reflection. This is done by modeling a sound-hard boundary at $y = 0.75$ m, or approximately one array diameter from the array center. The resultant ideal image source is located at (0,1.5,1.5) m, and is perfectly coherent with the true source. At the array center, the image signal leads the source signal by 135.8°. The level of the image signal at the array center is 97.0 dB. However, due to mild destructive interference the power of the sum of the source and its image is only 96.9 dB. The effect of the coherent interaction between the two sources is shown in Fig. A.12. The source-alone data are already plotted in Fig. A.9b. These variances can be compared to the image source alone data in Fig. A.12a. The summation of the two sources if they were incoherent with respect to each other is shown in Fig. A.12b. This is given as a comparison to the coherent case evaluated here, plotted in Fig. A.12c. The coherent interaction between the sources distorts the shape of the source lobes of the wavenumber transforms, and accentuates lobe structures at non-source wavenumbers.

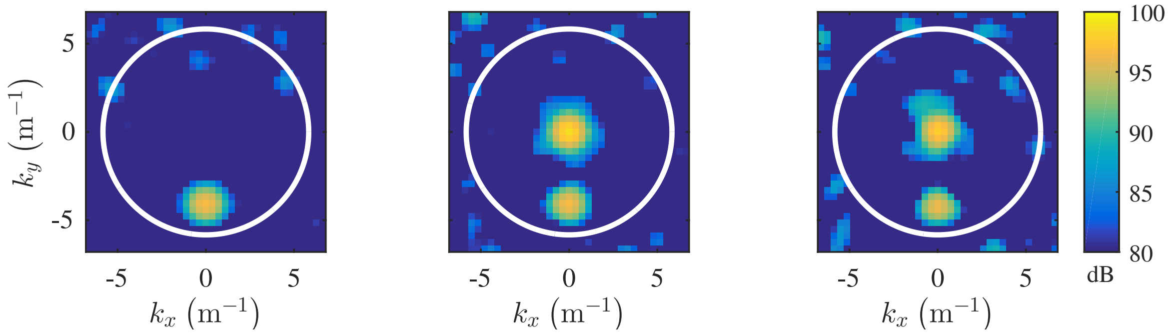

(a) isolated image source

(b) true source and image source, incoherent sum

(c) true source and image source, coherent sum

Figure A.12. Autovariance variation in wavenumber transform of array data due to interference between a source and reflection.

Deconvolution results are shown in Fig. A.13. Here, v drops below 10^{-13} with a corresponding value of $u = 7.30 \times 10^{-13}$ after 1.86×10^4 iterations, and is shown in Fig. A.14a (as a function of v, not iteration count). The incoherent method, again reported but not plotted, decreases below 10^{-13} after slightly more than 1.56×10^4 iterations. The corresponding u for the incoherent method is only 1.91×10^{-1}. As with the isolated point source, the coherent results show plane wave distributions residing within the angle integration boundaries, although the true source does not exactly match its isolated counterpart when the image source is present. The incoherent method again reduces the results to discrete plane waves.

Several integration metrics are considered for this case. First, the levels are computed for the source and image in isolation from each other, as well as for the combined acoustic field. This is done by computing two filter functions, Ψ_{source} and Ψ_{image}, using the method described in Appendix B. The isolated levels are computed by filtering the data separately with these functions. The combined level is computed by using $\Psi_{combined} = \Psi_{source} + \Psi_{image}$. This handling of the combined filter functions only works when source regions are well-separated in the wavenumber-frequency domain. Sources with wavenumber overlap must be

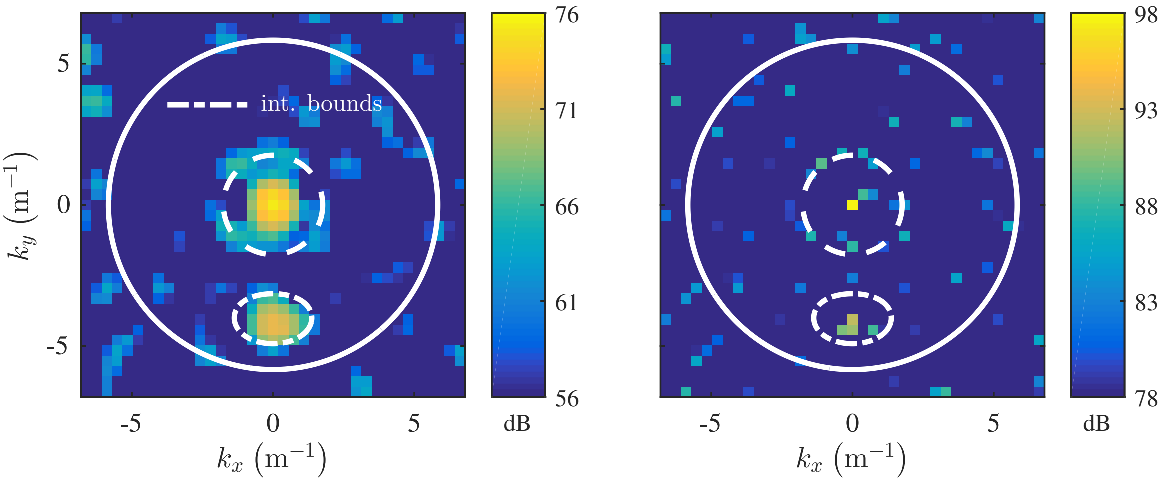

(a) coherent deconvolution

(b) incoherent deconvolution

Figure A.13. Variances from deconvolution of reflected point source data using $\Delta k_{()} = w/4$ spacing grid with both coherent and incoherent methods.

handled differently. Comparison is made to the appropriate array center levels. Array average levels are no longer plotted for the sake of clarity, as there is no obvious reason to choose the average over the center from results of the isolated point source case. Processing in comparison to the array average level for subsequent cases shows worse agreement when used as an alternative to the array center level.

The source level converges to 100.2 dB. While this is slightly above the array center level of 100 dB, it is in close agreement. The image level converges to 96.0 dB, which is 1 dB below the array center level of 97.0 dB. The combined level is calculated as 97.1 dB, slightly above the combined level at the array center of 96.9 dB. Overall these metrics are close to the array center value, although the deviation for the image source is somewhat larger than deviations seen for the isolated point source case. All three metrics appear to converge by $v = 10^{-6}$, which is again where v has achieved a two order-of-magnitude reduction after establishing a power law relationship with u.

Behavior of covariances is now considered. The covariance between the image and source can be calculated by filtering the data using the image and source filter functions on the respective baseline and conjugate wavenumber dimensions,

$$\tilde{Q}_{cov} = \sum \Psi_{image}\left(k_x, k_y\right) \Psi_{source}\left(k_\xi, k_\eta\right) \tilde{Q}\left(k_x, k_y, k_\xi, k_\eta\right). \tag{A.2}$$

The coherence-squared between the sources can then be computed as

$$\gamma^2 = \frac{\left|\tilde{Q}_{cov}\right|^2}{\tilde{Q}_{source} \times \tilde{Q}_{image}}. \tag{A.3}$$

The phase angle between the sources is simply the angle of $\tilde{Q}_{cov}$. The coherence function should be unity as the sources are perfectly coherent in a contamination-free field. The deconvolution process does not quite recover unity coherence, as shown in Fig. A.14c. However, the final value of $\gamma^2 = 0.98$ is extremely close to unity, and certainly sufficient to properly indicate the relationship between the sources. The computed phase angle converges to 136.7°. This is within 1° of the value of 135.8° at the array center. Were these values extracted from the raw transform of the data without deconvolution in an attempt to analyze the relationship of the source and its image, the coherence-squared is computed as a non-physical value of 1.11. This is due to the influence of negative powers from diagonal removal making $\tilde{P}$ an invalid covariance array. The phase angle is computed as 113.7°. Generating $\tilde{P}$ without diagonal removal yields the correct coherence-squared value of 1.00. However, the computed phase angle is 113.8°.

Integrated metrics for the incoherent solution are also computed at convergence. The source level is computed as 99.2 dB, while the image level is computed as 96.8 dB. Both of these levels are close to their respective level at the array center. However, the combined level is computed as 101.2 dB, over 4 dB higher than the combined level at the array center. As would be expected, without the covariance information relating the sources, they cannot be summed properly.

Appendix B Integration weighting function

The wavenumber filtering technique used in this work begins by defining a boundary curve in the wavenumber-frequency domain. This curve may follow the acoustic radiation boundary and thus be used to separate acoustic and subsonic hydrodynamic data. It may also follow a curve used to isolate energy arriving from a region of directions of arrival. As an example, consider using the acoustic radiation circle defined by $|k| = k_0$ as the filter boundary where the region within the circle is the desired signal. This circle is plotted for $f = 1$ kHz and $c_0 = 343$ m/s in Fig. B.1. Two grid points on a coarse wavenumber grid are considered. These grid points are illustrated as two-dimensional boxes centered on the grid point coordinates with dimensions determined by $\Delta k_{()}$. The first grid box lies entirely within the acoustic radiation domain and thus has a weighting of $\Psi(0,0) = 1$. The second grid box lies on the boundary, so the weighting is determined the ratio of the area of the grid box within the circle to the total grid box area. In this example, this ratio is approximately 0.33. The function $\Psi(-0.735, -2.94)$ for this grid point is thus the square root of the area ratio, or $\sqrt{0.33}$. This means the contribution of the variance of this grid point to the summation, where $\Psi(k_x, k_y) = \Psi(k_\xi, k_\eta)$ in Eq. (A.1), is simply this area ratio multiplied by the variance, or $0.33 \times \tilde{Q}(-0.735, -2.94, -0.735, -2.94)$. The contribution of the first grid point is $\tilde{Q}(0,0,0,0)$. The contribution of the covariance between these two grid points, $\Psi(0,0) \times \Psi(-0.735, -2.94) \times \tilde{Q}$ from Eq. (A.1), is $\sqrt{1} \times \sqrt{0.33} \times \tilde{Q}(0, 0, -0.735, -2.94)$. The conjugate covariance between these two points receives the same weighting. The weighting for any covariance with one component outside of the radiation domain is thus

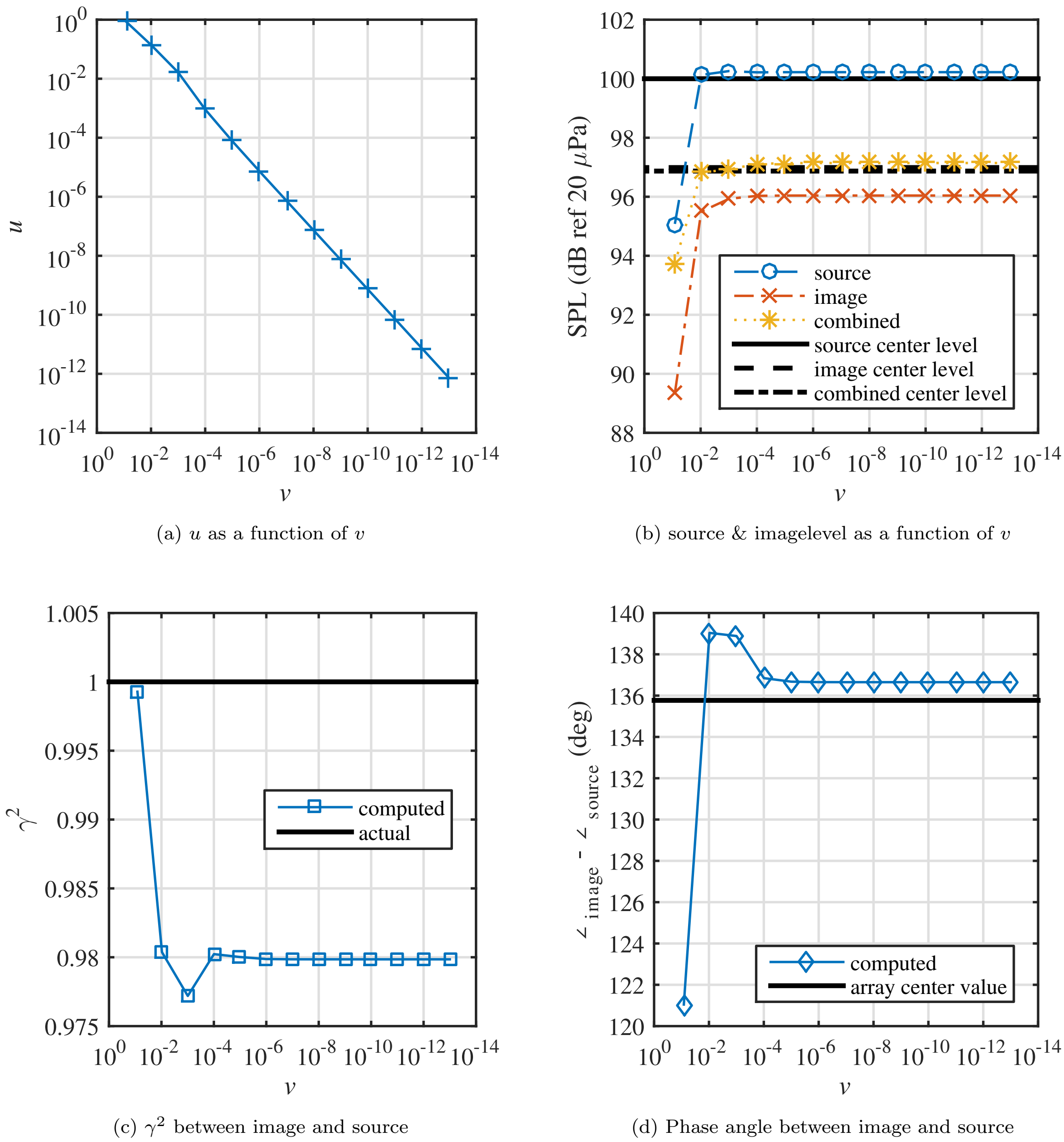

(a) u as a function of v

(b) source & imagelevel as a function of v

(c) γ^2 between image and source

(d) Phase angle between image and source

Figure A.14. Convergence behavior and metrics evaluation of the coherent solution technique for the point source with reflection simulation.

zero.

For general curve selection to isolate waves from a region of directions of arrival, a geometric argument is used where waves are projected from the source of interest to the circle defining the outer ring of microphones of the array. This projection defines a cone of directions of energy propagation. This direction of energy propagation can be related to wave vector angles which then yield an integration region when projected onto the plane defined by $k_z = 0$. When no flow is present the angles are the same. When flow is present they differ, and the relationships are addressed in Appendix C. To capture energy leaked to adjacent wavenumber-frequency bins for directions of arrival between grid points, the integration bounds are expanded by Δk in the k-direction normal to the initial calculation of the integration bounds. This expanded integration bound is then used to define $\Psi\left(k_x, k_y\right)$ using the above-described boundary treatment.

As an aside, note that the direction of arrival calculation establishes a paradoxical situation for wavenumber-frequency data analysis with regard to array design. A larger array yields a smaller array main lobe in the wavenumber-frequency domain, improving resolution. However, a smaller array will have a smaller observation cone and thus provide improved resolution and isolation of sources in post-deconvolution analysis. These effects should be considered as a design trade off for any arrays which may be used specifically for wavenumber-frequency analysis of aeroacoustic data acquired near a source or set of sources.

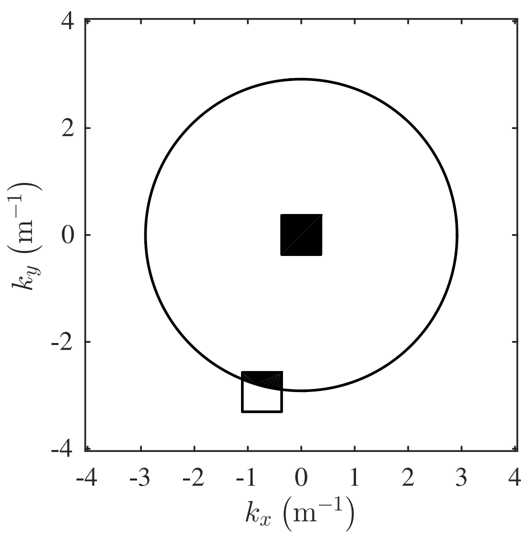

Figure B.1. Example of area-based weighting scheme for wavenumber filtering.

Appendix C Radiation domain and angle relations in the presence of mean flow

The homogeneous wave equation for pressure in a moving medium with constant velocity U in the x-direction is given by [34]

$$\frac{\partial^2 p}{\partial t^2} + 2U\frac{\partial^2 p}{\partial x \partial t} + U^2\frac{\partial^2 p}{\partial x^2} - c_0^2\nabla^2 p = 0. \tag{C.1}$$

This can be refactored in terms of Mach number as

$$\frac{1}{c_0^2}\frac{\partial^2 p}{\partial t^2} + 2\frac{M}{c_0}\frac{\partial^2 p}{\partial x \partial t} - \left[\left(1 - M^2\right)\frac{\partial^2 p}{\partial x^2} + \frac{\partial^2 p}{\partial y^2} + \frac{\partial^2 p}{\partial z^2}\right] = 0. \tag{C.2}$$

Assuming the pressure signal is space-time harmonic,

$$p = \tilde{p}e^{j2\pi(ft - k_x x - k_y y - k_z z)}, \tag{C.3}$$

Eq. (C.3) can be substituted into Eq. (C.2) and the resultant divided by the right-hand side of Eq. (C.3) and $4\pi^2$, yielding

$$-k_0^2 + 2Mk_0k_x + \left(1 - M^2\right)k_x^2 + k_y^2 + k_z^2 = 0. \tag{C.4}$$

Setting $k_z = 0$ to establish the appropriate k_x/k_y plane, the boundary of the radiation domain is determined by

$$k_y^2 = k_0^2 - 2Mk_0k_x - \left(1 - M^2\right)k_x^2. \tag{C.5}$$

When no flow is present, this boundary collapses to the traditional acoustic radiation circle. When there is mean flow, the boundary curve is an ellipse with semi-major and semi-minor axes of $k_0/\left(1 - M^2\right)$ and $k_0/\sqrt{1 - M^2}$, respectively. Foci are located at $(k_x, k_y) = (0, 0)$ and $(k_x, k_y) = \left(-2M \times k_0/\left(1 - M^2\right), 0\right)$. Note that here Mach number should include the sign of the flow direction.

Eq. (C.4) can be re-arranged to establish the dispersion relation of frequency f as a function of wavenumber vector $\vec{k}$. The dispersion equation is

$$f\left(\vec{k}\right) = Mc_0k_x + c_0\sqrt{k_x^2 + k_y^2 + k_z^2}. \tag{C.6}$$

Two velocity vectors can be computed from the dispersion equation. The phase velocity vector defines the speed and direction in which planes of constant phase move forward, and has a direction which matches the wave vector. The group velocity vector defines the speed and direction in which energy propagates [35]. When $U = 0$ for this wave equation, the two vectors are identical. However, for an anisotropic wave equation such as this one for non-zero U, they are not. The phase velocity vector is given by

$$\vec{v}_p = \frac{f}{\left|\vec{k}\right|}\frac{\vec{k}}{\left|\vec{k}\right|}. \tag{C.7}$$

The group velocity vector is given by

$$\vec{v}_g = \nabla_{\vec{k}} f. \tag{C.8}$$

Substituting Eq. (C.6) into Eq. (C.7) and defining the spherical coordinates

$$\begin{aligned} k_x &= \left|\vec{k}\right| \cos\theta_p \\ k_y &= \left|\vec{k}\right| \sin\theta_p \cos\phi_p \\ k_z &= \left|\vec{k}\right| \sin\theta_p \sin\phi_p \end{aligned} \tag{C.9}$$

yields

$$\vec{v}_p = c_0 \left(1 + M\cos\theta_p\right) \left(\cos\theta_p \hat{e}_x + \sin\theta_p \cos\phi_p \hat{e}_y + \sin\theta_p \sin\phi_p \hat{e}_z\right). \tag{C.10}$$

Substituting Eq. (C.6) into Eq. (C.8) similarly yields

$$\begin{aligned} \vec{v}_g &= c_0 \left(M_0 + \cos\theta_p\right) \hat{e}_x + c_0 \sin\theta_p \cos\phi_p \hat{e}_y + c_0 \sin\theta_p \sin\phi_p \hat{e}_z \\ &= \left|\vec{v}_g\right| \cos\theta_g \hat{e}_x + \left|\vec{v}_g\right| \sin\theta_g \cos\phi_g \hat{e}_y + \left|\vec{v}_g\right| \sin\theta_g \sin\phi_g \hat{e}_z. \end{aligned} \tag{C.11}$$

For the filtering process described, θ_g and ϕ_g are assumed known and θ_p and ϕ_p are desired. $|\vec{v}_g|$ is first found in terms of the phase velocity angles. This can then be used with the $\hat{e}_x$ component of Eq. (C.11) to find

$$\theta_p = \theta_g - \sin^{-1}\left(-M\sin\theta_g\right). \tag{C.12}$$

The azimuth angle relationship is then found through the $\hat{e}_y$ and $\hat{e}_z$ components of Eq. (C.11) as

$$\phi_p = \phi_g. \tag{C.13}$$

The final element required to project propagation angles onto the $k_z = 0$ plane is the magnitude of the wave vector. This is found from Eq. (C.6) as

$$\left|\vec{k}\right| = \frac{k_0}{1 + M\cos\theta_p}. \tag{C.14}$$